Available online at www.sciencedirect.com

ScienceDirect

Underground Space 27 (2026) 216–235

www.keaipublishing.com/undsp

Research Paper

A novel fractal-order elasto-visco-plastic creep damage model and its engineering-scale creep parameter determination method

Qingzhe Cui [a], Fei Wu [a,*], Jianfeng Liu [b], Jie Chen [a], Cunbao Li [c], Renbo Gao [a], Shuo Gao [a], Yu Wang [a], Huiqing Liu [a], Tao Ren [d]

[a] *State Key Laboratory for the Coal Mine Disaster Dynamics and Controls, Chongqing University, Chongqing 400044, China*
[b] *State Key Laboratory of Hydraulics and Mountain River Engineering, Sichuan University, Chengdu 610065, China*
[c] *State Key Laboratory of Intelligent Construction and Healthy Operation and Maintenance of Deep Underground Engineering, College of Civil and Transportation Engineering, Shenzhen University, Shenzhen 518060, China*
[d] *China Railway Changjiang Transport Design Group Co., Ltd., Chongqing 400020, China*

Received 18 July 2025; received in revised form 11 September 2025; accepted 15 October 2025
Available online 21 January 2026

Abstract

The effective prediction and evaluation of the long-term stability of deep-buried tunnels are crucial for tunnel design, construction, and operation. The creep model is key to predicting time-dependent behavior, and the accuracy of time-dependent deformation predictions is determined by the creep parameters. This paper introduces a novel fractal-order elasto-visco-plastic creep damage (FEVPD) model that incorporates long-term strength into the damage evolution equation within the framework of continuum damage mechanics. The model effectively captures the three-stage creep behavior of various rock types and predicts their creep lifespans under different stress levels. The FEVPD model was implemented in FLAC3D using C++. Additionally, in determining the creep parameters of rock at the engineering scale to address the high computational cost of parameter inversion, an improved genetic algorithm was developed with adaptive perturbation, elitism, and dynamic mutation mechanisms. Application to field monitoring data from the Jinping II hydropower station tunnel demonstrated that the FEVPD model improved the prediction accuracy of time-dependent deformation by 32.68% compared to the classical Burgers–Mohr (CVISC) model. The enhanced inversion method also reduced the final error by 26.0% and 22.7% for the FEVPD and CVISC models, respectively, compared with the standard algorithm. Finally, this model was used to predict the long-term stability of the tunnel. The results provide a reliable and efficient framework for modeling and predicting creep behavior in deep rock engineering.

Keywords: Fractal-order derivatives; Creep model; Numerical simulation; Parameter inversion; Improved genetic algorithm

1 Introduction

The time-dependent behavior of rock under high in-situ stress is a primary hazard in deep tunnels, where delayed deformation could potentially trigger cracking and, in severe cases, instability or collapse (Cui et al., 2025c; Kong et al., 2023; Liu et al., 2023, 2025; Wang et al., 2025; Yang et al., 2023). Therefore, the development of constitutive models that can accurately predict the time-dependent deformation of rock is essential for assessing the long-term stability of deep tunnels. However, two gaps continue to limit practice—prediction and validation: establishing creep models that reliably forecast time-dependent deformation behavior and validating such models objectively and efficiently in engineering settings.

A fractional-order derivative is a form of differentiation between an integer-order derivative and an integer-order integral (Herrmann, 2014). It can describe nonlocal

* Corresponding author.
E-mail address: wufei3616@cqu.edu.cn (F. Wu).
Peer review under the responsibility of Tongji University

https://doi.org/10.1016/j.undsp.2025.10.009

phenomena and behaviors in complex systems. Studies (Gao et al., 2022; Liang et al., 2024; Lyu et al., 2021) have shown that fractional derivatives perform satisfactorily in characterizing the decay stage of rock creep because they can capture the memory effect of rocks and power-law-type creep and describe rock creep behavior with fewer parameters (Kabwe et al., 2020a). However, fractional elements have practical limitations: (1) their mathematical form increases the computational cost and reduces efficiency (Kilbas et al., 2006); (2) parameter interpretation can be ambiguous because a small set of parameters is expected to govern both decay and steady-state responses, limiting applicability when steady-state creep is weak; (3) they struggle to reproduce the viscoelastic recovery observed in graded loading–unloading creep tests (Wang et al., 2022; Zhao et al., 2017a, 2017b).

In the accelerated stage, modelling commonly relies on damage mechanics. Liang et al. (2024) incorporated temperature into the damage evolution equation in a negative exponential form and proposed a 3D thermo-mechanical creep model for salt and validated its accuracy and applicability experimentally. Zheng et al. (2024) introduced the elastic modulus into the damage evolution equation and established a creep damage model for layered sand–mudstone that effectively captures the anisotropy and progressive failure characteristics of the surrounding rock of a tunnel. Yang et al. (2024) adopted the Kachanov damage evolution law to develop a damage creep model, treating pre-existing flaws as material damage and effectively capturing the time-dependent behavior of fractured rock. Zhou et al. (2022) established a nonlinear damage–hardening creep model for deep soft rock by incorporating both damage and hardening mechanisms and validated its capability to predict the onset of accelerated failure and long-term strength. T. Li et al. (2024) proposed a creep damage constitutive model by introducing damage state functions based on the Gurson model to capture both steady and accelerated creep stages and validated it through creep–acoustic emission tests on saturated phyllite. However, a key physical constraint is often overlooked: when the stress level σ is at or below the long-term strength σ_L, the creep lifespan should, in principle, diverge; many existing formulations do not reproduce this threshold-consistent behavior.

The constitutive model determines the form of time-dependent deformation of the rock, whereas the magnitude is controlled by the creep parameters. At the experimental scale, these parameters are typically identified by nonlinear fitting of laboratory data to verify the applicability and accuracy of the model (Cui et al., 2025a; Gong et al., 2025; Wu et al., 2022). However, at the engineering scale, the mapping from creep parameters to deformation becomes highly nonlinear and implicit and is affected by complex stress fields, irregular geometries, and rock-mass heterogeneity; thus, laboratory-based parameters often fail to transfer directly. Consequently, some studies adopt lab-derived values or manually tune parameters to match field observations, which compromises objectivity and weakens the scientific rigor of model validation. Therefore, inverse analysis has become a common tool for identifying the mechanical parameters in large-scale rock engineering (An et al., 2020; Chang et al., 2023; Ghorbani et al., 2021; Mahmoudi & Rajabi, 2020; Sun et al., 2021). However, most applications target elastic or strength parameters, and research on creep parameter inversion remains limited because full-scale time-dependent simulations are computationally expensive and challenging to optimize.

Based on the above analysis, some urgent scientific problems that must be addressed in the study of rock creep models remain: (1) fractional-order creep models encounter challenges of computational burden, parameter interpretability, and recovery reproduction; (2) several damage-based accelerated-creep formulations do not honor the σ_L threshold for creep lifespan; (3) engineering-scale validation often relies on subjective parameter transfer or manual tuning; (4) the high computational cost of creep inversion limits its practical applications.

Therefore, this paper introduces a fractal-order Kelvin body into the creep constitutive model, organically combines σ_L with the Kachanov damage evolution law, and establishes a novel fractal-order elasto-visco-plastic creep damage (FEVPD) model that accurately represents the delayed deformation characteristics of rock. The rationality and applicability of the model were verified using experimental creep data for marble, sandstone, and salt rock. The program code of the FEVPD model in FLAC3D was successfully achieved using the Visual Studio 2019 (VS2019) platform and C++ language. Furthermore, to objectively evaluate the time-dependent mechanical behavior of the FEVPD model at the engineering scale, this paper proposes a novel improved genetic algorithm (GA) integrated into FLAC3D for parameter inversion. The optimal parameters of the FEVPD and Burgers–Mohr (CVISC) models were obtained from the background of the tunnel of the Jinping II hydropower station, which was used to compare and analyze the excellence of the FEVPD model. Finally, the model was applied to predict the long-term stability of the deeply buried tunnel.

2 Establishment of fractal-order model

2.1 Viscoplastic component considering damage evolution

The viscoplastic deformation behavior of rock is often described using a Newtonian body in parallel with a St. Venant body. The constitutive equation is represented as

$$\dot{\varepsilon}_{vp} = \frac{\sigma - \sigma_s}{\eta_2}, \tag{1}$$

where $\dot{\varepsilon}_{vp}$ represents the first-order time derivative of the viscoplastic strain, and σ_s represents the yield strength of the rock. For creep problems in rocks, the yield strength in a St. Venant body can be replaced by the long-term

strength. η_2 represents the viscosity coefficient of the viscoplastic component.

Moreover, the accumulation of viscoplastic deformation in rock is also a process of continuous initiation, development, and expansion of microfractures in the rock. According to Lemaitre's strain equivalence principle (Lemaitre, 1996), the strain caused by a damaged material under full stress is equivalent to the strain caused by an undamaged material under effective stress, and the damage variable D is introduced into it. Therefore, Eq. (1) can be written as

$$\dot{\varepsilon}_{vp} = \frac{\sigma - \sigma_L}{\eta_2(1-D)}. \tag{2}$$

According to the Kachanov damage evolution law (Kachanov, 1958), the evolution of rock creep damage can be expressed as

$$\dot{D} = \kappa\left(\frac{\sigma - \sigma_L}{1-D}\right)^{\gamma}, \tag{3}$$

where κ and γ are the intrinsic parameters of rock materials: κ linearly scales the time rate of damage accumulation in the Kachanov damage law, and γ quantifies the sensitivity of creep lifespan to the distance from σ_L (stress-sensitivity index). $\dot{D}$ is the first-order time derivative of the damage variable. Solving this differential equation yields

$$D = 1 - \{-(1+\gamma)[\kappa(\sigma - \sigma_L)^{\gamma}t + C]\}^{\frac{1}{1+\gamma}}, \tag{4}$$

where C is the undetermined coefficient, and t represents the creep time. Rock creep damage accumulates continuously, and the duration for it to reach full failure (0 to 1) is termed the creep failure time (t_R). Integrating the boundary condition $\begin{cases} D=0, & t=0 \\ D=1, & t=t_R \end{cases}$ into Eq. (4), the rock creep damage evolution equation is obtained as

$$D = 1 - \left(1 - \frac{t}{t_R}\right)^{\frac{1}{(\gamma+1)}}, \tag{5}$$

where

$$t_R = \left[\kappa(\gamma+1)\left(\frac{\sigma - \sigma_L}{\sigma^*}\right)^{\gamma}\right]^{-1}, \tag{6}$$

where σ^* denotes the unit stress, introduced to eliminate dimensional influences, with a unit of MPa. Notably, as implied by Eq. (6), when multiple single-level creep-to-failure tests are conducted at $\sigma > \sigma_L$, the parameters κ and γ can be directly identified by fitting the creep failure times across different stress levels.

According to Eq. (6), Fig. 1 shows that under the new method, the creep failure time tends to infinity when the stress level is at or below σ_L, whereas it decreases nonlinearly when the stress exceeds σ_L. This highlights the threshold role of σ_L in rock creep and provides a more accurate description of stress dependence. In contrast, traditional methods yield creep lifespans that are insensitive to stress variation and fail to capture the σ_L threshold.

Thus, the viscoplastic component considering damage evolution is shown in Fig. 2.

When the stress is maintained constant at σ_0, substituting Eq. (5) into Eq. (2) yields the following creep equation:

$$\varepsilon = \begin{cases} 0, & \sigma_0 < \sigma_L \\ \frac{\sigma_0 - \sigma_L}{\eta_2}\frac{(\gamma+1)t_R}{\gamma}\left[1 - \left(1 - \frac{t}{t_R}\right)^{\frac{\gamma}{(\gamma+1)}}\right], & \sigma_0 \geq \sigma_L \end{cases}. \tag{7}$$

2.2 Viscoelastic component with fractal order

As mentioned above, owing to the limitations of the fractional-order Newtonian body in describing the viscoelastic behavior of rock, this paper introduces a fractal-

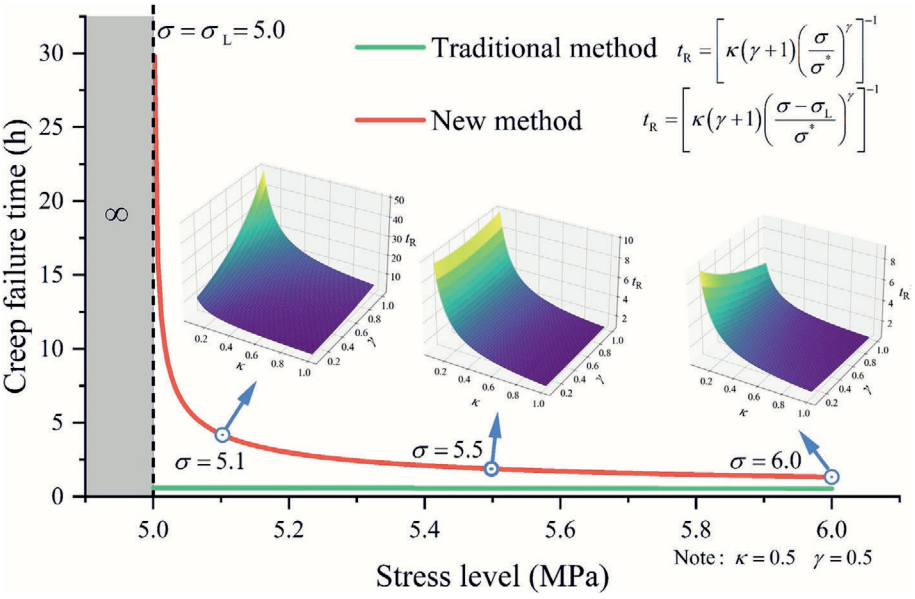

Fig. 1. Influence of parameters on the creep failure time of rock.

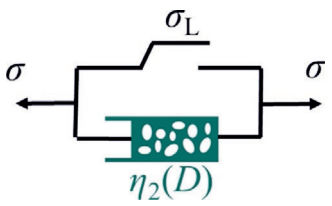

Fig. 2. Viscoplastic component considering damage evolution.

order viscoelastic element and combines it in parallel with a Hooke body to represent the decay creep of a rock, as shown in Fig. 3.

The fractal-order derivative can be defined as

$$\frac{\mathrm{d}f(t)}{\mathrm{d}t^{\xi}} = \lim_{t' \to t} \frac{f(t) - f(t')}{t^{\xi} - t'^{\xi}}, \tag{8}$$

where ξ represents the order of the fractal-order derivative (0–1). From Eq. (8), the derivative functions as a local operator without a convolution integral. However, through scale transformation $t = t^{\xi}$ (Kilbas et al., 2006), it can be reformulated as a classical integer derivative. The effectiveness of this approach has been verified in previous studies (Cai et al., 2016; Kabwe et al., 2020b; H. Li et al., 2024). Accordingly, the evolution equation of the fractal-order viscous element can be written as

$$\eta^{\xi}(t) = \frac{\eta_1^{\xi}}{\xi} t^{1-\xi}. \tag{9}$$

where η_1^{ξ} denotes the viscosity coefficient of the viscoelastic body (defined on the ξ-order time scale). In addition, from Eq. (9), the fractal-order derivative can be considered a time-dependent nonlinear generalization of the viscosity coefficient.

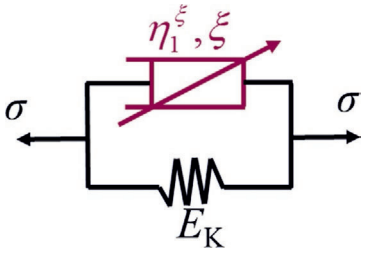

Fig. 3. Fractal-order viscoelastic component.

Table 1 shows the difference between the integer-order, fractal-order, and fractional-order elements when describing the time-dependent deformation in the Maxwell and Kelvin components. The fractal order does not require complex series summation and has a simpler form. Figure 4 presents the comparison between the fractal-order and fractional-order Kelvin models under different orders (ξ) with the classical Kelvin model, using the parameters E_K = 520.2 GPa and η_K = 6562.2 GPa·h, which are derived from the fitting results at 135.7 MPa for the FEVPD model. It can be observed that, when ξ approaches 0, both models exhibit good instantaneous deformation characteristics and can describe the instantaneous elastic behavior of rock. When $\xi = 1$, both models are completely consistent with the classical Kelvin model in describing time-dependent deformation. When $0 < \xi < 1$, the deformation of the fractal-order Kelvin body is slightly greater than that of the fractional-order Kelvin model, but both have the same curve shape. This demonstrates that the fractal-order Kelvin body is as effective as the fractional-order Kelvin body in characterizing the decay creep behavior of rock.

The creep equation of the viscoelastic component consisting of a fractal-order viscous element in parallel with a Hooke body can be expressed as

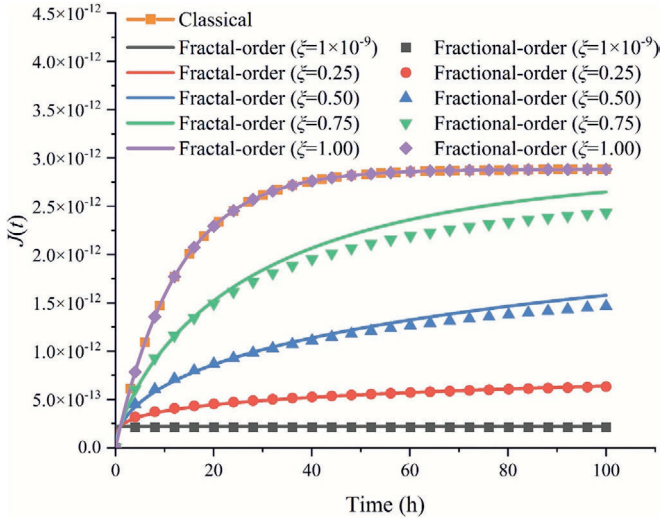

Fig. 4. Comparison of Kelvin bodies of different types and orders.

Table 1
Comparison of creep modulus of Maxwell and Kelvin bodies based on integer, fractal, and fractional orders.

Model	Integer order	Fractal order	Fractional order
Maxwell	$J(t) = \frac{1}{E_M} + \frac{t}{\eta_M}$	$J(t) = \frac{1}{E_M} + \frac{t^{\xi}}{\eta_M}$	$J(t) = \frac{1}{E_M} + \frac{1}{\eta_M} \frac{t^{\xi}}{\Gamma(1+\xi)}$
Kelvin	$J(t) = \frac{1}{E_K}\left[1 - \exp\left(-\frac{E_K t}{\eta_K}\right)\right]$	$J(t) = \frac{1}{E_K}\left[1 - \exp\left(-\frac{E_K t^{\xi}}{\eta_K}\right)\right]$	$J(t) = \frac{1}{\eta_K} \sum_{k=0}^{\infty} \frac{\left(-\frac{E_K}{\eta_K}\right)^k t^{\xi(1+k)}}{\xi(1+k)\Gamma[(1+k)\xi]}$

Note: $J(t)$ is the creep modulus, E_M is the Maxwell modulus, E_K is the Kelvin modulus, η_M is the Maxwell viscosity, η_K is the Kelvin viscosity, k is the non-negative integer (value: 100 (J. Wu et al., 2023)), ξ is the fractal/fractional-order derivative order, and Γ is the Gamma function.

$$\varepsilon_{ve} = \frac{\sigma_0}{E_K}\left[1 - \exp\left(-\frac{E_K t^{\xi}}{\eta_1^{\xi}}\right)\right] \quad (0 \le \xi \le 1), \tag{10}$$

where ε_{ve} represents the viscoelastic strain. Throughout the remainder of this paper, $0 \le \xi \le 1$ is applied.

2.3 Creep equation of the FEVPD model

In creep studies, rock deformation consists of instantaneous and delayed components. The former can be represented by a Hooke body that describes elastic behavior, whereas the latter can be effectively characterized by the previously introduced viscoplastic and viscoelastic components. In summary, a novel FEVPD model is established in this paper by connecting the Hooke body in series with the previously proposed viscoplastic and viscoelastic components, as shown in Fig. 5, where K and G_1 denote the bulk modulus and shear modulus of the Hookean body, respectively, and G_2 represents the shear modulus of the fractal-order viscoelastic component.

As shown in Fig. 5, the strains generated by each component are denoted ε_{ij}^{e}, ε_{ij}^{ve}, and ε_{ij}^{vp}, respectively. Two assumptions are made: (1) The mechanical properties of the rocks are isotropic. (2) Whether a rock undergoes time-dependent damage is strictly controlled by whether the stress level surpasses σ_L. Additionally, owing to human-induced disturbances and other factors, deep surrounding rocks are typically subjected to three-dimensional stress states. Therefore, the theoretical equations should be extended to a three-dimensional form. However, because of space limitations, the 1D theoretical equations of the model are not discussed in detail.

Consequently, the strain tensor component of the FEVPD model can be expressed as

$$\varepsilon_{ij} = \varepsilon_{ij}^{e} + \varepsilon_{ij}^{ve} + \varepsilon_{ij}^{vp}, \tag{11}$$

Under a 3D stress state, the stress tensor component (σ_{ij}), strain tensor component (ε_{ij}), deviatoric stress tensor component (S_{ij}), and deviatoric strain tensor component (e_{ij}) have the following relationships:

$$\begin{cases} \sigma_{ij} = S_{ij} + \sigma_m \delta_{ij}, \\ \varepsilon_{ij} = e_{ij} + \varepsilon_m \delta_{ij}, \end{cases} \tag{12}$$

where δ_{ij} is the Kronecker delta, σ_m is the mean stress, and ε_m is the mean strain.

Based on the generalized Hooke's law,

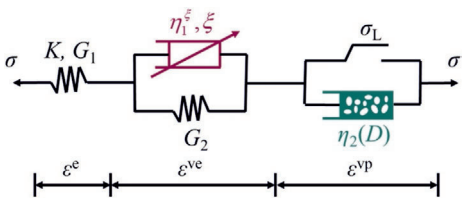

Fig. 5. Schematic of the FEVPD model.

$$\begin{cases} S_{ij} = 2G_1 e_{ij}, \\ \sigma_m = 3K\varepsilon_m. \end{cases} \tag{13}$$

The constitutive equation of Hooke body can be written as

$$\varepsilon_{ij}^{e} = \frac{1}{2G_1} S_{ij} + \frac{1}{3K}\sigma_m \delta_{ij}. \tag{14}$$

Under normal-temperature conditions, scholars generally believe that creep is primarily caused by shear stress (Alessandro & Eurípedes, 2023; F. Wu et al., 2023). Based on Eqs. (9) and (13), the 3D viscoelastic creep equation can be derived as follows:

$$\varepsilon_{ij}^{ve} = \frac{S_{ij}}{2G_2}\left[1 - \exp\left(-\frac{G_2}{\eta_1^{\xi}} t^{\xi}\right)\right], \tag{15}$$

The 3D viscoplastic creep constitutive relationship is governed by the yield criterion and flow rule. Based on Perzyna's viscoplastic constitutive model (Perzyna, 1966), and combining Eqs. (7) and (13), the 3D creep equation of the viscoplastic component can be expressed as

$$\varepsilon_{ij}^{vp} = \frac{1}{2\eta_2}\left\langle \phi\left(\frac{F}{F_0}\right)\right\rangle \frac{\partial Q}{\partial \sigma_{ij}}\left\{\frac{(\gamma+1)t_R}{\gamma}\left[1 - \left(1 - \frac{t}{t_R}\right)^{\frac{\gamma}{(\gamma+1)}}\right]\right\}, \tag{16}$$

where

$$\left\langle \phi\left(\frac{F}{F_0}\right)\right\rangle = \begin{cases} 0 & (F < 0), \\ \phi\left(\frac{F}{F_0}\right) & (F \ge 0), \end{cases} \tag{17}$$

where F represents the yield function, F_0 is the initial reference value of the yield function, and Q denotes the plastic potential function. $\phi(\bullet)$ follows a power function form, typically with an exponent of 1 (Zienkiewicz & Cormeau, 1974).

By substituting Eqs. (14)–(16) into Eq. (11), the three-dimensional creep equation of the FEVPD model can be obtained as

$$\varepsilon_{ij} = \begin{cases} \frac{1}{2G_1}S_{ij} + \frac{1}{3K}\sigma_m\delta_{ij} + \frac{1}{2G_2}\left[1 - \exp\left(-\frac{G_2}{\eta_1^{\xi}}t^{\xi}\right)\right]S_{ij} & (F < 0), \\ \frac{1}{2G_1}S_{ij} + \frac{1}{3K}\sigma_m\delta_{ij} + \frac{1}{2G_2}\left[1 - \exp\left(-\frac{G_2}{\eta_1^{\xi}}t^{\xi}\right)\right]S_{ij} + & \\ \frac{1}{2\eta_2}\left(\frac{F}{F_0}\right)\frac{\partial Q}{\partial \sigma_{ij}}\left\{\frac{(\gamma+1)t_R}{\gamma}\left[1 - \left(1 - \frac{t}{t_R}\right)^{\frac{\gamma}{(\gamma+1)}}\right]\right\} & (F \ge 0). \end{cases} \tag{18}$$

Adopting the non-associated flow law, the Mohr–Coulomb yield criterion is employed as the plasticity criterion. The tensile yield function F^t, shear yield function F^s, shear plasticity potential function Q^s, and tensile plasticity potential function Q^t have the following forms:

$$\begin{cases} F^s = \sigma_1 - \sigma_3 N_\varphi + 2c\sqrt{N_\varphi}, \\ Q^s = \sigma_1 - \sigma_3 N_\psi, \\ F^t = \sigma^t - \sigma_3, \\ Q^t = -\sigma_3, \end{cases} \tag{19}$$

where $N_\varphi = (1 + \sin\varphi)/(1 - \sin\varphi)$, $N_\psi = (1 + \sin\psi)/(1 - \sin\psi)$, c, φ, and ψ denote the cohesion, friction, and

dilation angles, respectively. σ_1 and σ_3 represent the first and third principal stresses, and σ^t represents the tensile strength.

Assuming $F_0 = 1$ and focusing on the shear failure, the 3D creep equation for the FEVPD model under the conventional triaxial test is derived by incorporating Eq. (19) into Eq. (18):

$$\varepsilon_{11} = \begin{cases} \frac{\sigma_1-\sigma_3}{3G_1} + \frac{\sigma_1+2\sigma_3}{9K} + \frac{\sigma_1-\sigma_3}{3G_2}\left[1 - \exp\left(-\frac{G_2}{\eta_1^{\xi}}t^{\xi}\right)\right] & (F < 0), \\ \frac{\sigma_1-\sigma_3}{3G_1} + \frac{\sigma_1+2\sigma_3}{9K} + \frac{\sigma_1-\sigma_3}{3G_2}\left[1 - \exp\left(-\frac{G_2}{\eta_1^{\xi}}t^{\xi}\right)\right] + \\ \frac{\sigma_1-\sigma_3 N_\varphi - 2c\sqrt{N_\varphi}}{2\eta_2}\left\{\frac{(\gamma+1)t_R}{\gamma}\left[1 - \left(1 - \frac{t}{t_R}\right)^{\frac{\gamma}{(\gamma+1)}}\right]\right\} & (F \geq 0). \end{cases} \tag{20}$$

3 Model calibration

3.1 Parameter identification

To validate the rationality and applicability of the FEVPD model, it was fitted to the creep test data of three different types of rocks. The experimental data were obtained for marble (Chen et al., 2013), sandstone (Yin et al., 2024), and salt rock (He et al., 2022). Table 2 presents the basic mechanical parameters, where c, φ, and Poisson's ratio μ were obtained based on common values and calculations.

The FEVPD model parameters were identified in Origin using Eq. (20) and the Levenberg–Marquardt algorithm (Marquardt, 1963). The parameters for the marble, sandstone, and salt rock are presented in Tables 3–5. Figure 6 illustrates the parameter identification results for marble, sandstone, and salt rock. The FEVPD model indicates high agreement with the indoor test data, with R^2 values of the curves being very close to 1. This confirms that the FEVPD model effectively captures the creep characteristics of the different rock types.

Figure 7 shows the variation curves of the fractal-order coefficients of the rocks with the stress levels. As the stress increases, the fractal-order coefficient also increases. This indicates that the rheological properties of the rocks are increasing and the fractal-order viscous element of the Kelvin model is evolving towards the integer-order element.

3.2 Parameter sensitivity analysis

To explore the influence of uncommon material parameters (such as the fractal-order coefficient ξ and material parameters κ and γ) on the FEVPD model time-dependent performance, a sensitivity analysis was conducted on these parameters. The model parameters of marble under a stress level of 135.7 MPa from Section 3.1 were used as the basic parameters, as listed in Table 6.

Figure 8 shows the effects of different ξ, κ, and γ on the FEVPD model. The figure shows that κ and γ determine the creep lifespan. As κ and γ increase, the material enters the accelerated creep stage earlier, resulting in a shorter creep lifespan. The fractal-order coefficient ξ determines the deformation rate of the material in a finite time. When $t < 1$ h, the deformation of the material decreases continuously as ξ increases. When $t \geq 1$ h, the deformation of the material increases continuously as ξ increases. It is noteworthy that the maximum deformation of the fractal-order Kelvin component is controlled by the magnitude of G_2.

3.3 Prediction of creep lifespan

Based on Eq. (6) and Tables 2–5, the trends of creep lifespan with stress levels are plotted for marble, sandstone, and salt rock, as shown in Fig. 9. The creep lifespan of the three rocks predicted by the FEVPD model decreases nonlinearly with increasing stress level, which is consistent with the above analysis results. Notably, salt rock has stronger rheological properties than marble and sandstone, exhibits good creep characteristics under lower stress levels, and maintains a relatively long creep lifespan when the stress level is significantly higher than its long-term strength.

4 Numerical implementation

4.1 Creep model compilation

Appendix A provides a detailed derivation of the finite difference formulation of the FEVPD model. Subsequently, the numerical code of the constitutive model was developed in C++ on the VS2019 platform. Figure 10 shows a detailed flowchart of the program implementation process for the constitutive model. Finally, the dynamic link library (.dll) of the constitutive model was generated using the VS2019 platform, which enabled its integration into FLAC3D.

4.2 Verification of numerical program

An oedometer test (ITASCA, 2017) can clearly reveal the constitutive relationship of the model; therefore, this method was adopted to verify the correctness of the numer-

Table 2
Basic mechanical parameters of three different types of rocks.

Rock type	Confining pressure (MPa)	σ_L (MPa)	c (MPa)	φ (°)	μ
Marble	0	130.1	27.00	45	0.20
Sandstone	10	58.9	10.08	32	0.26
Salt rock	0	8.0	3.18	13	0.35

Table 3
Parameters for marble.

Deviatoric stress (MPa)	G_1 (GPa)	G_2 (GPa)	η_1^{ξ} (GPa·h$^{\xi}$)	η_2 (GPa·h)	K (GPa)	ξ	γ	κ
115.3	22.47	258.9	2376.7	–	29.97	0.348	–	–
120.4	22.24	224.0	3962.7	–	29.65	0.435	–	–
125.5	21.95	393.1	2769.4	–	29.27	0.612	–	–
130.6	21.35	262.5	1827.7	2183.6	28.47	0.711	0.901	5.36×10^{-3}
135.7	20.29	173.4	2187.4	308.0	27.06	0.959	0.901	5.36×10^{-3}

Note: Experimental data are from Chen et al. (2014).

Table 4
Parameters for sandstone.

Deviatoric stress (MPa)	G_1 (GPa)	G_2 (GPa)	η_1^{ξ} (GPa·h$^{\xi}$)	η_2 (GPa·h)	K (GPa)	ξ	γ	κ
10	18.96	29.7	15.9	–	33.18	0.923	–	–
25	19.20	40.6	17.8	–	33.60	0.925	–	–
40	19.92	67.5	64.0	–	34.85	0.945	–	–
55	19.96	80.5	50.4	–	34.92	0.952	–	–
70	18.30	196.6	55.0	1143.6	32.02	0.960	0.1809	6.63×10^{-2}

Note: Experimental data are from Yin et al. (2024).

Table 5
Parameters for salt rock.

Deviatoric stress (MPa)	G_1 (GPa)	G_2 (GPa)	η_1^{ξ} (GPa·h$^{\xi}$)	η_2 (GPa·h)	K (GPa)	ξ	γ	κ
4.66	0.396	0.011	3.05	11.29	1.187	0.271	–	–
9.32	0.494	0.186	2.76	32.40	1.482	0.570	3.2	2.43×10^{-5}
14.0	0.287	0.214	0.56	13.21	0.862	0.867	3.2	2.43×10^{-5}
16.5	0.120	3.446	0.63	1.12	0.361	0.960	3.2	2.43×10^{-5}

Note: Experimental data are from He et al. (2022).

ical implementation of the FEVPD model in this section. A numerical validation was conducted using the marble parameters at 135.7 MPa (Table 6). Figure 11 compares the numerical solution of the FEVPD model with the theoretical solution and indoor test results. The numerical solution of the model closely matches the theoretical solution in all stages (decay creep, steady-state creep, and accelerated creep) and shows minimal error compared with the indoor test results. This demonstrates the successful implementation of the FEVPD model.

5 Model application and parameter confirmation method

5.1 Numerical modeling of the deeply buried tunnel

The Jinping II hydropower station tunnel, at a depth of 2500 m, was used to further validate the applicability of the FEVPD model. A half model (60 m × 50 m × 80 m) was built, consisting of 265 380 zones and 279 563 nodes (Fig. 12). The initial crustal stresses in the x, y, and z directions were −36.091, −28.296, and −44.708 MPa, respectively (Chen & Feng, 2008), and the displacement boundary conditions with normal constraints were applied except for the top plane. The tunnel monitoring points are shown on the right side of Fig. 12.

5.2 Method of determining model parameters at the engineering scale

Owing to the inherent differences in the time and space scales between laboratory tests and field conditions, the creep parameters obtained from experiments are often not directly applicable to engineering-scale simulations (Bonini et al., 2007; Cui et al., 2025b; Luo et al., 2021). Therefore, adopting a systematic and objective parameter inversion method not only provides a reliable basis for evaluating the performance of constitutive models but also enables accurate prediction of the long-term stability of deep tunnels. As a representative intelligent optimization technique, the GA (Holland, 1975) has a strong global search capability and is well-suited for solving complex, nonlinear, and multiparameter optimization problems. It has been widely applied in geotechnical engineering for high-dimensional parameter inversions (Feng et al., 2006; Li et al., 2025; Majdi & Beiki, 2010; Wang et al., 2004; Zheng et al., 2020).

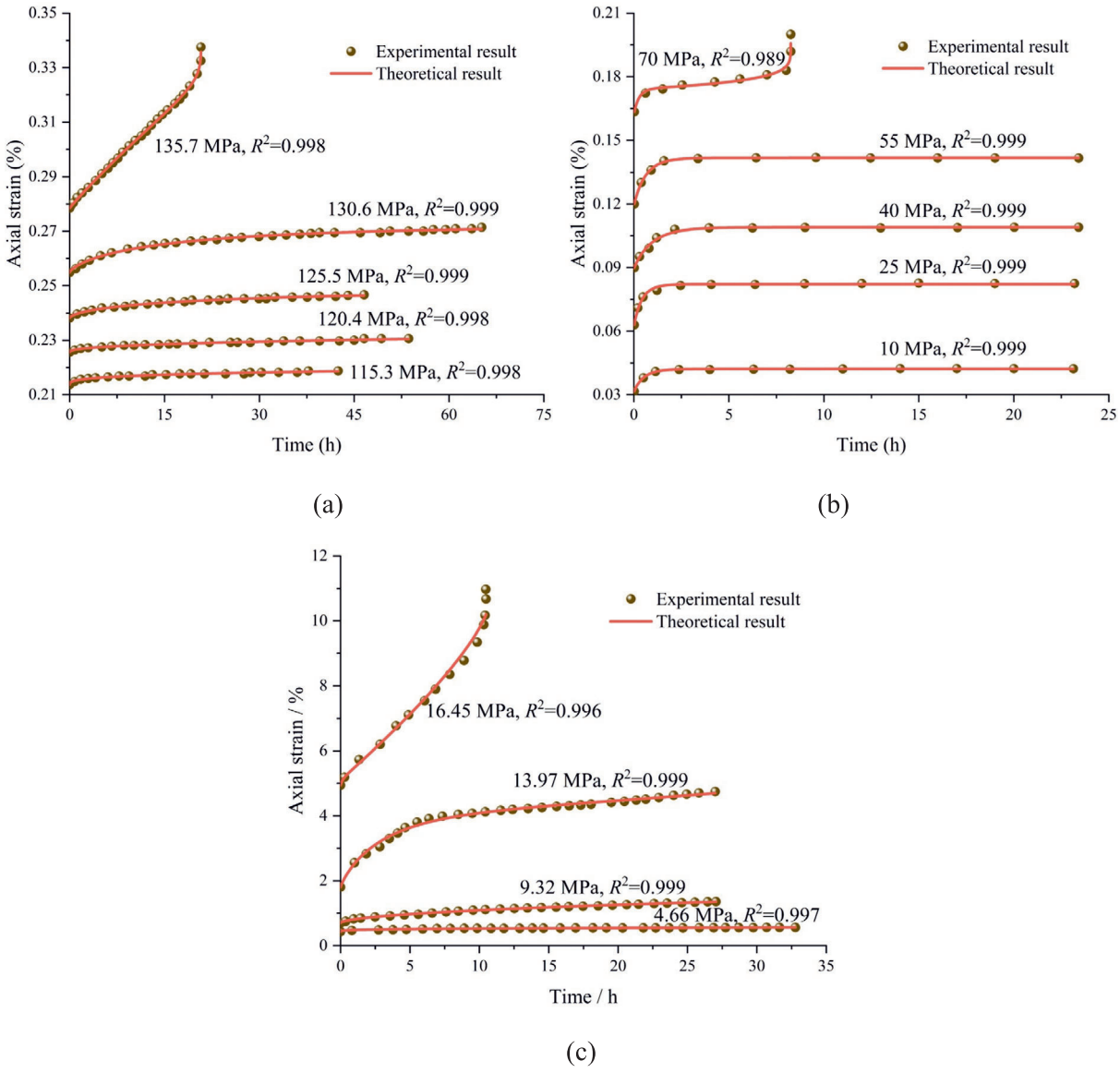

Fig. 6. Comparison of theoretical curves of the FEVPD model with indoor test and data for three different types of rocks. (a) Marble, (b) sandstone, and (c) salt rock.

However, for parameter inversion tasks involving large-scale creep simulations of deep rock masses, each numerical evaluation is computationally intensive and time-consuming. A standard GA typically relies on large populations and many generations to ensure global search effectiveness. However, under realistic engineering constraints, such high computational demand is often impractical. Moreover, the standard GA tends to suffer from local optima and unstable convergence when limited to a small number of iterations. Thus, improving the balance between the optimization accuracy and computational efficiency is a key challenge in large-scale engineering parameter inversion. Hence, this paper proposes an improved GA, whose process is shown in a program flowchart (Fig. 13).

(1) An adaptive perturbation inheritance mechanism

To avoid premature convergence and improve the fine-tuning capability near high-quality solutions, an adaptive perturbation inheritance mechanism is introduced. Instead of directly copying the parent parameters to the offspring during crossover, each parameter is slightly perturbed based on its frequency in the current population. More frequently appearing parameter values receive smaller perturbations, whereas rarer values are more strongly perturbed. This adaptive perturbation enables the algorithm to maintain population diversity while intensifying the search for promising regions.

Mathematically, for a given parameter y with a value y_i in the i-th individual and its occurrence count $f(y_i)$ within the current population, the offspring value y_i' is defined as

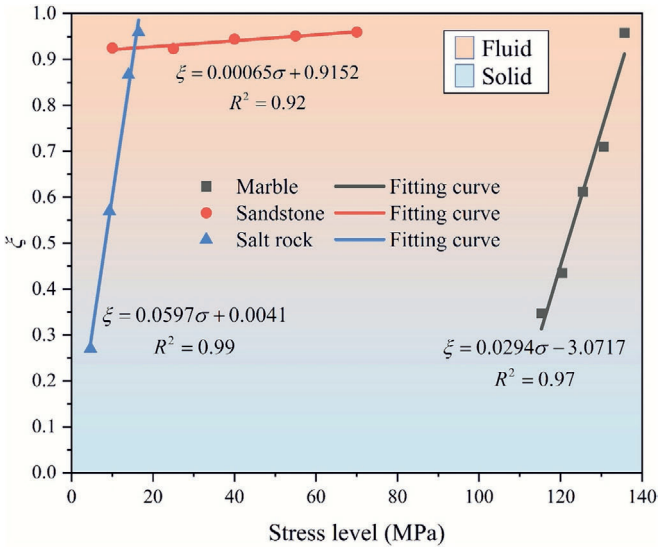

Fig. 7. Variation curves of fractal-order coefficients of rocks with stress levels.

$$y_i' = \begin{cases} y_i, & f(y_i) = 1, \\ y_i + \frac{m}{f(y_i)}(r - 0.5)\Delta\theta, & f(y_i) > 1, \end{cases} \tag{21}$$

where $\Delta\theta$ is the maximum allowable perturbation amplitude, $r \in (0,1)$ is a uniformly distributed random variable controlling direction and magnitude, and m denotes the population size of each generation.

To avoid unnecessary perturbations when the population is still far from convergence, this mechanism is activated only when both the mean and minimum errors of the current generation fall below the predefined thresholds.

(2) An elitism strategy

To ensure that high-quality solutions are not lost during stochastic operations such as crossover or mutation, an elitism strategy is employed. In each generation, the best-performing individual is explicitly preserved and carried over to the next generation without modification.

(3) A dynamic mutation adjustment strategy based on real-time convergence indicators

To prevent premature stagnation in scenarios where the population fails to meet the convergence criteria, a dynamic mutation adjustment strategy is introduced. When either the mean or the minimum error in the current generation exceeds a predefined threshold, the mutation rate is increased in proportion to the mean error. This amplifies the exploratory behavior of the algorithm and encourages movement out of the suboptimal regions. Conversely, when both the mean and minimum errors satisfy their respective thresholds, the mutation rate is restored to its initial value.

Based on these enhancements, a customized inversion framework was developed by integrating the GA with FLAC3D through Python programming. Field monitoring data from the Jinping II hydropower station (Zhang et al., 2019) were used as the inversion targets. Several key parameters controlling the time-dependent deformation were encoded into gene sequences, and their fitness was evaluated through numerical simulations. The roulette wheel selection method was applied with an initial mutation rate of 0.05, which was dynamically adjusted based on the error evolution from the previous generation. A total of $n = 100$ generations evolved with $m = 50$ individuals per generation.

Selecting an appropriate error function (Samaniego et al., 2020) is crucial for the performance and improvement of the GA. In this study, the L_{2P} error was used as the error function because it enables the inversion to be based on the entire deformation history rather than on a single value, thereby providing a more comprehensive reflection of the time-dependent performance of the constitutive model.

$$L_{2P} = \sqrt{\frac{\sum_{l=1}^{4}\left(W_l \sum_{i=1}^{v}\left(x_{i,\mathrm{sim}}^{j-k} - x_{i,\mathrm{mon}}^{j-k}\right)^2\right) + W_{\mathrm{Mean}} \sum_{i=1}^{v}\left(x_{i,\mathrm{sim}}^{\mathrm{Mean}} - x_{i,\mathrm{mon}}^{\mathrm{Mean}}\right)^2}{\left(\sum_{l=1}^{4} W_l + W_{\mathrm{Mean}}\right) v}}, \tag{22}$$

where $x_{i,\mathrm{sim}}^{\mathrm{Mean}}$ and $x_{i,\mathrm{mon}}^{\mathrm{Mean}}$ represent the mean convergence displacements of the numerical simulation results and in-situ monitoring data, respectively. $x_{i,\mathrm{sim}}^{j-k}$ and $x_{i,\mathrm{mon}}^{j-k}$ represent the convergence displacements between the measurement points from the numerical simulation results and in-situ monitoring data, respectively. j–k denotes the indices of the two monitoring points. W represents the weighting coefficients for different types of convergence deformation (W_1, W_2, W_3, and W_4 are set to 1, whereas W_{Mean} is set to 4), and v denotes the total number of measurement points along a line (set to 21).

Owing to the high computational demand of this method, the numerical model is simplified to a two-dimensional plane problem with a unit depth (y-axis) (the error with the three-dimensional model of Section 5.1 was verified to be less than 0.5%), which significantly reduces the time required for the inversion of the parameters. To reduce computational cost, a dynamic time-step

Table 6
Basic parameters for parameter sensitivity analysis.

Deviatoric stress (MPa)	G_1 (GPa)	G_2 (GPa)	η_1^{ξ} (GPa·h$^{\xi}$)	η_2 (GPa·h)	K (GPa)	ξ	γ	κ
135.7	20.29	173.4	2187.4	308.0	27.06	0.959	0.901	5.36×10^{-3}

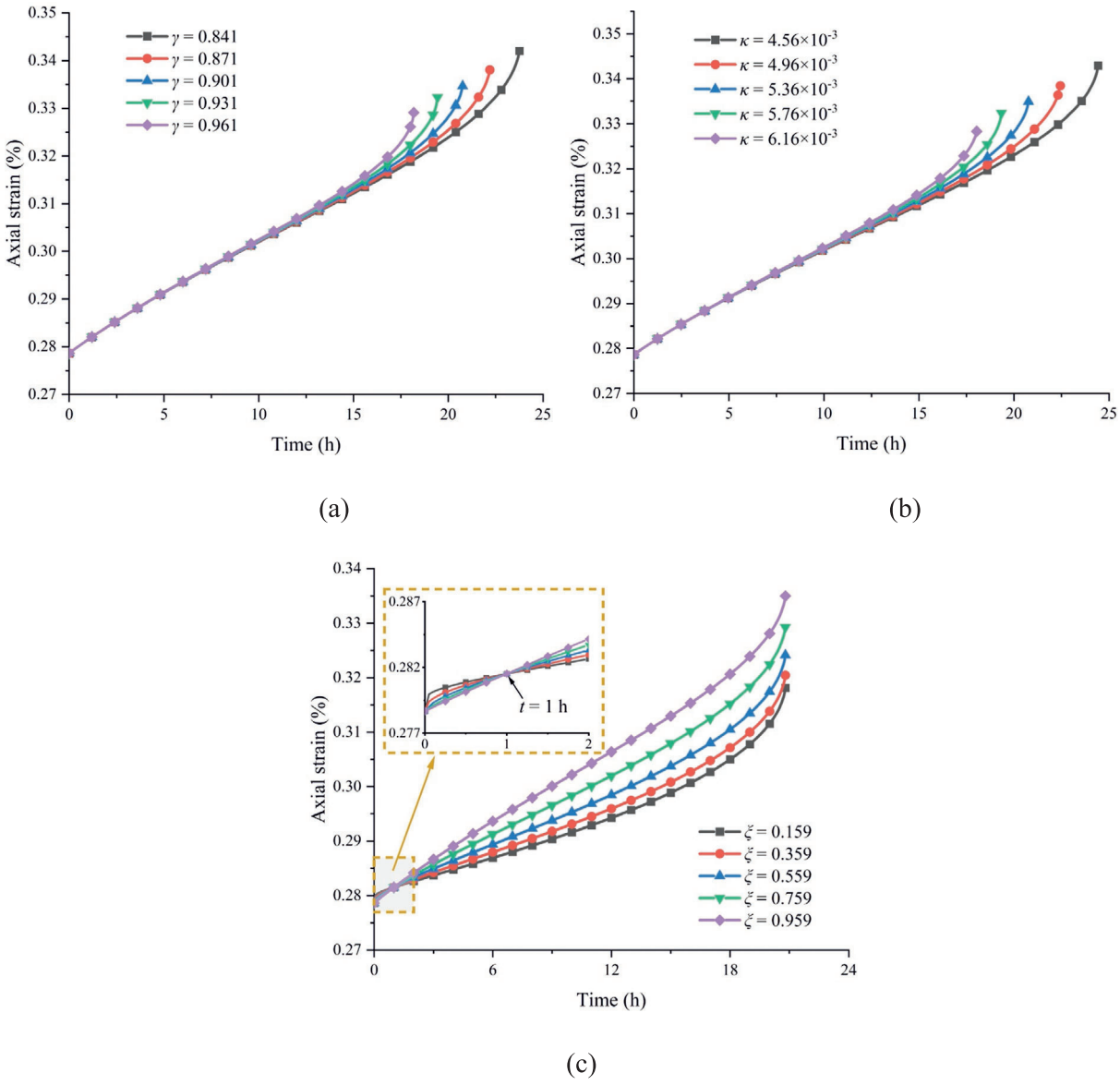

Fig. 8. Effects of different parameters on the FEVPD model. (a) γ, (b) κ, and (c) ξ.

strategy is adopted in the simulation. In this approach, smaller time steps are used when the creep rate is high, and larger time steps are applied during low-rate periods. This strategy helps balance the computational efficiency and result accuracy. After applying the dynamic time-step strategy, the temporal axis of the deformation history became non-uniform. Therefore, adjacent linear interpolation is employed to extract deformation values at consistent time intervals for comparison and parameter inversion.

To better demonstrate the performance of the FEVPD model in describing time-dependent deformation, it was compared with the CVISC model embedded in FLAC3D. The basic parameters used in the numerical calculations for both models are listed in Table 7. In the table, G_1 and K were taken from the fitting results of the FEVPD model at 135.7 MPa, γ and κ were obtained by appropriate attenuation on the basis of the fitting results, and c, φ, ρ, and σ^t were taken from the relevant reference (Hou et al., 2024). The accuracy of the creep simulation depended not only on the model and parameters but also on the stress field, which was derived from instantaneous mechanical calculations. Both analyses adopted the Mohr–Coulomb criterion, but with different strength parameters: peak strength (c = 10 MPa) for the instantaneous analysis and long-term strength (c = 6 MPa) for the creep simulation.

5.3 Algorithm inversion result

Figure 14 compares the inversion performances of the standard and improved GA applied to the CVISC and FEVPD creep models. In all four cases, the L_{2P} error decreases progressively with increasing generations, indicating successful convergence and effective parameter optimization. Notably, the

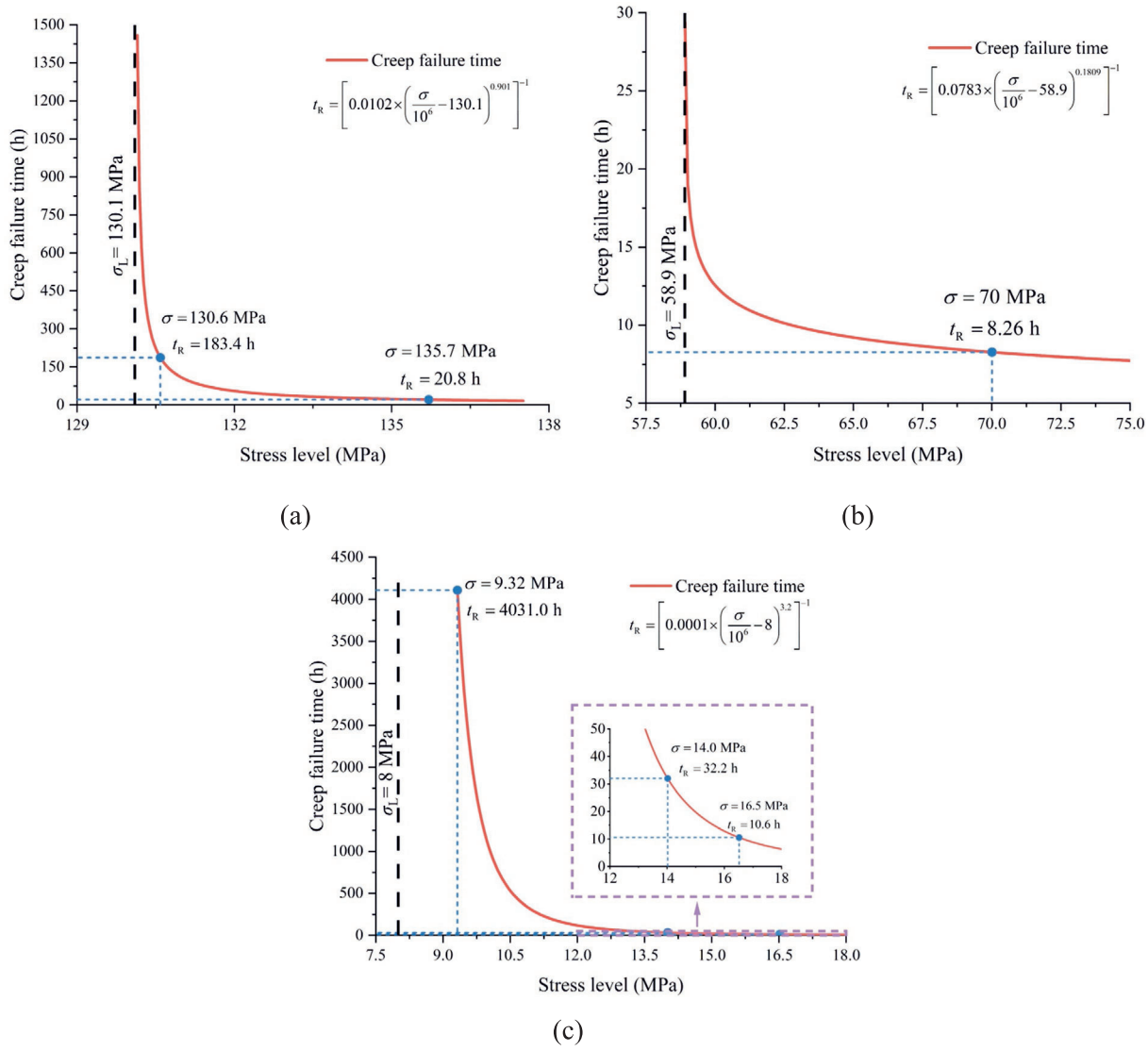

Fig. 9. Variation curves of creep lifespan with stress levels for the three types of rocks. (a) Marble, (b) sandstone, and (c) salt rock.

error declines most sharply during the first 30 generations, after which the convergence trend gradually levels off.

The improved GA exhibits significant advantages over the standard GA in terms of both convergence speed and final accuracy. For the CVISC model, the improved GA reduces the final L_{2P} error from 1.326 to 1.025 mm, representing a 22.7% improvement. Similarly, for the FEVPD model, the error decreases from 0.931 to 0.689 mm, corresponding to a 26.0% reduction. These results highlight the enhanced efficiency and robustness of the improved GA, particularly under the constraint of high computational cost in large-scale parameter inversion tasks.

In addition to the optimization method, the choice of the constitutive model also plays a critical role. The FEVPD model consistently outperformed the CVISC model, regardless of the algorithm used. When paired with the improved GA, the FEVPD model achieved the lowest final error (0.689 mm), representing a 32.68% decrease compared with the CVISC model under the same conditions (1.025 mm). This suggests that the FEVPD model has a stronger capacity for capturing the time-dependent mechanical response of deep rock masses.

The final optimized parameters for both models are listed in Table 8, along with the corresponding L_{2P} errors. To further evaluate the superiority of the improved GA in the inversion of the creep model parameters, a more detailed comparison is provided in Appendix B.

5.4 Comparison of numerical simulation results

Figure 15 shows the numerical simulation results for the local convergence deformation of the tunnel using the FEVPD and CVISC models. The convergence deformation between monitoring points 2 and 3 is denoted as 2-3, and similarly for the other points. The numerical simulation results of the FEVPD model exhibited a higher degree of

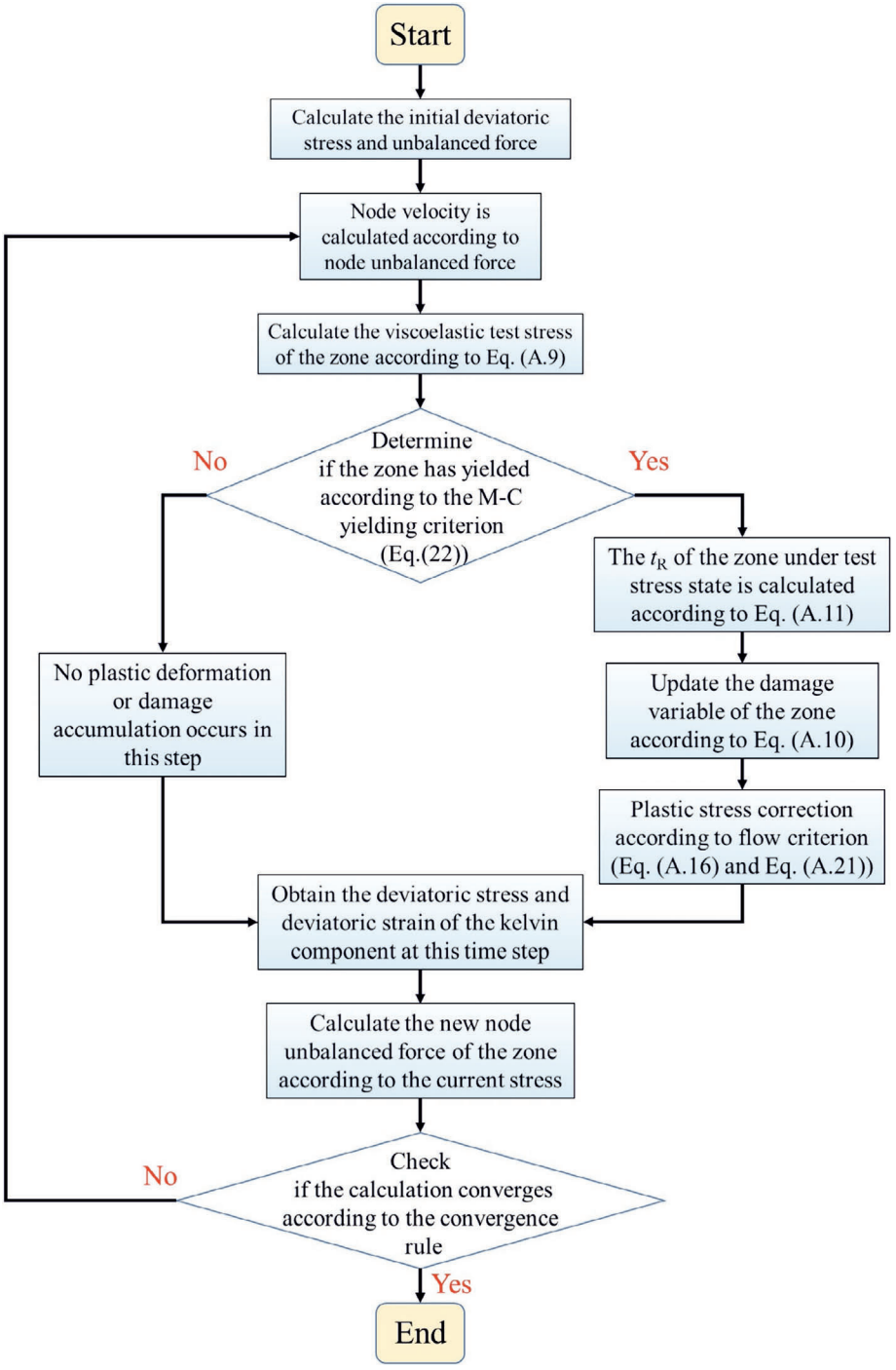

Fig. 10. Flowchart of the numerical implementation of the FEVPD model.

fit for each local convergence deformation, particularly at locations 1-3 and 4-5. Compared with the CVISC model, the FEVPD model demonstrates more significant advantages in describing the time-dependent deformation at 2-3, 2-5, and 1-3. For example, at 2-5, the degree of fit of the FEVPD model is 0.976, whereas that of the CVISC model is only 0.933.

Figure 16 shows a comparison of the creep simulation results of the FEVPD model with those of other models (Kabwe et al., 2020a; Zhang et al., 2019) for describing the mean convergent deformation of the tunnel. Although the FEVPD model effectively describes the local convergence deformation, it also provides an accurate prediction of the mean convergence deformation, which has received significant attention in engineering studies (Barla et al., 2012; Debernardi & Barla, 2009). Its R^2 value reaches 0.998, which is significantly higher than those of the other models.

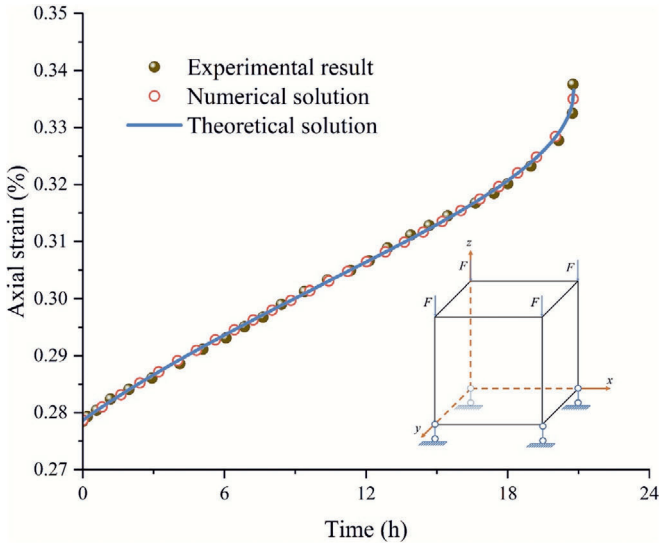

Fig. 11. Comparison of indoor test data with the theoretical and numerical solutions of the FEVPD model.

Figure 17 illustrates the 20-day evolution of the total plastic zone volume and first principal stress for the FEVPD and CVISC models. The total plastic zone volume of the CVISC model changes rapidly within a very short time (0.03 d) after the onset of creep and then almost stabilizes at a constant value. In contrast, the plastic zone volume of the FEVPD model initially increases rapidly and then gradually slows following a power-law function while also exhibiting a steadily increasing trend. Additionally, the first principal stress of the CVISC model fluctuates irregularly within a small range. However, the first principal stress of the FEVPD model gradually decreases in a power-law form until it stabilizes. This phenomenon can be attributed to the fact that the CVISC model cannot describe the viscoplastic deformation and ignores the time dependence of the material during plastic deformation. Whether the CVISC model undergoes failure is determined only by the magnitude of the stress rather than by time. Notably, for Point 1 of the FEVPD model, the first principal stress gradually decreases from −33.92 to −22.42 MPa over time. It can be considered that, at the engineering scale, the creep process of the surrounding rock corresponds to a continuous stress release.

5.5 Long-term stability prediction

Although the time-dependent deformation of the surrounding rock may not be significant in the early stage, its gradual accumulation over time can pose severe risks, potentially leading to structural damage or even overall tunnel failure (Zhao et al., 2025). The FEVPD model was employed to evaluate the long-term stability of a deeply buried tunnel to explore this time-dependent behavior. As shown in Fig. 18, the plastic zone volume increases from 1358 m^3 at day 0 to 2777 m^3 at day 20, indicating a rapid expansion characteristic of the decay creep stage. From day 20 to day 70, the volume grows slowly from 2777 to 2952 m^3, reflecting a relatively stable steady-state creep stage with relatively small deformation accumulation. However, beginning at day 70, the plastic zone expands rapidly and nonlinearly, reaching 4104 m^3 by day 80, which marks the onset of the accelerated creep stage. Meanwhile, the convergence deformation in sections 2-5 and 4-5 increases significantly after day 72, whereas sections 2-3 and 1-3 show delayed responses. This indicates that the

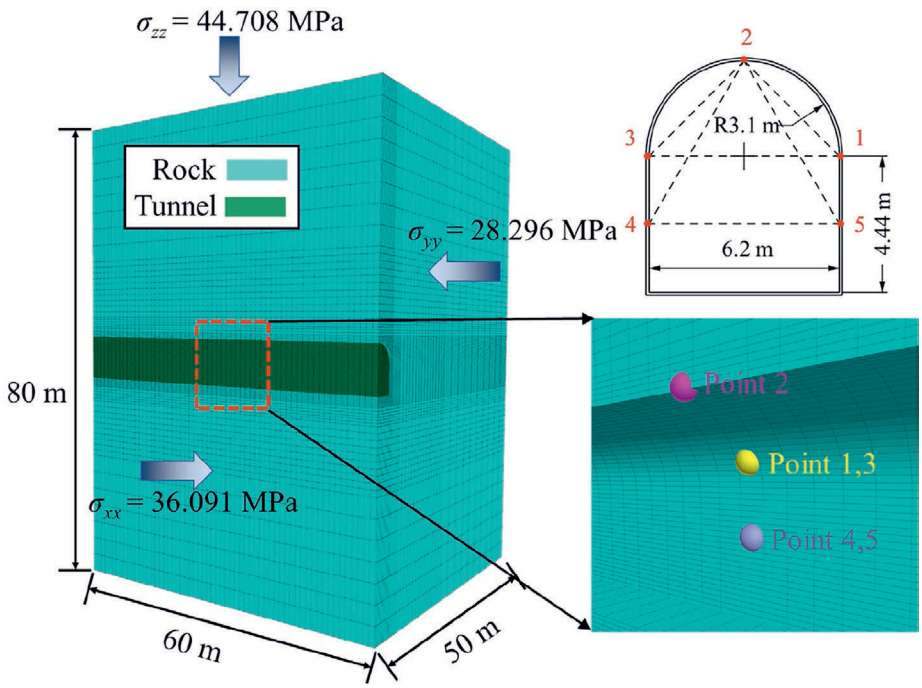

Fig. 12. Numerical model and measurement point locations.

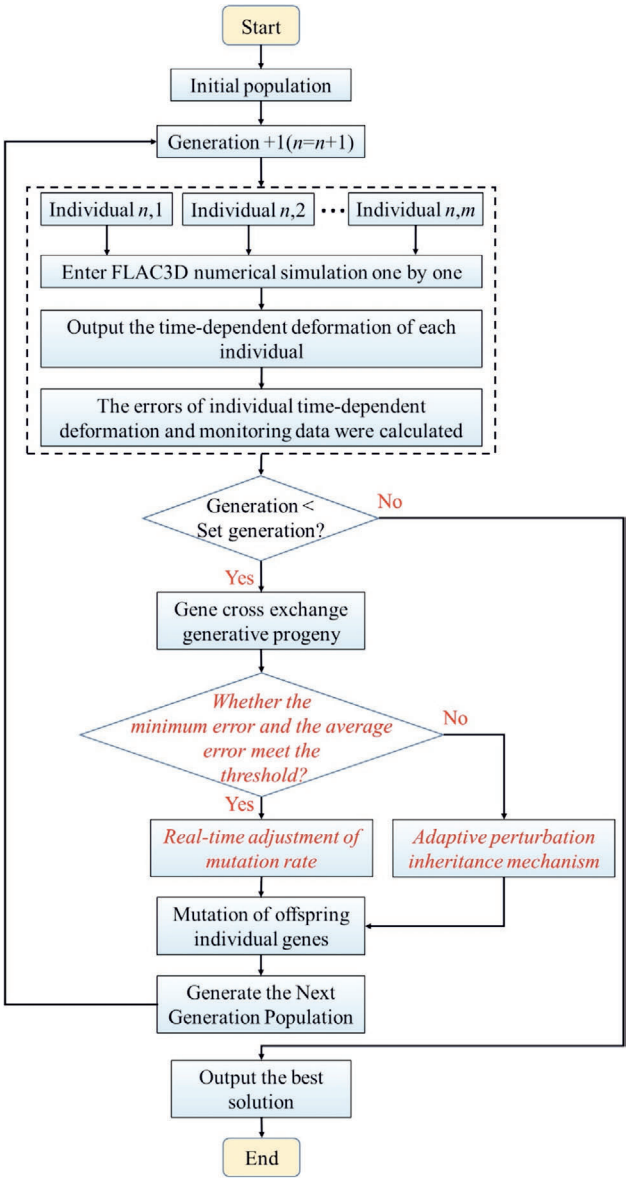

Fig. 13. Improved GA-FLAC3D flowchart.

large deformation of the tunnel most likely starts from local areas, which, in turn, leads to overall tunnel instability and failure. Because no support lining is applied in the simulation, the results reflect a worst-case scenario, in which insufficient or delayed support may result in creep-induced collapse.

6 Conclusions

This paper introduces a novel fractal-order elasto-visco-plastic creep damage (FEVPD) model that incorporates the fractal-order theory and continuum damage mechanics to characterize the three-stage creep behavior of rock. The main conclusions are as follows:

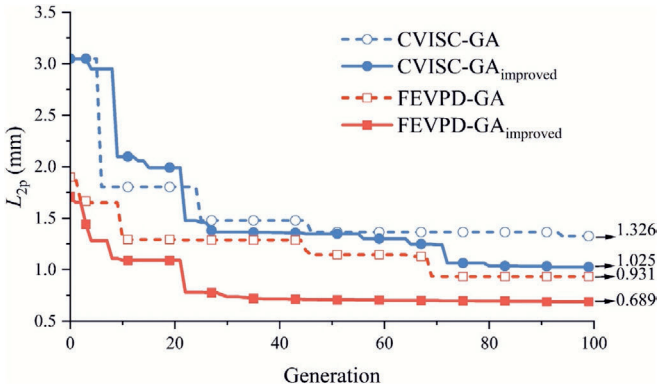

Fig. 14. Convergence comparison of standard and improved GA applied to CVISC and FEVPD models.

(1) A fractal-order Kelvin body describing the decay–creep stage of the rock was established by the scaling transformation of time. Compared with the fractional-order viscous element, the fractal-order Kelvin body more accurately reproduces the rock's power-law time-dependent mechanism and can effectively describe the viscoelastic recovery characteristics of the rock after sudden unloading under long-term stress.
(2) Based on Lemaitre's strain equivalence principle and the Kachanov damage evolution law, this paper introduces long-term strength into the damage evolution equation, redefining the creep damage evolution mechanism of a viscoplastic body. This improvement resolves the discontinuity problem of creep lifespan (t_R) at $\sigma \to \sigma_L$ of the damage evolution law of traditional viscoplastic bodies. The proposed viscoplastic body effectively characterizes the nonlinear accelerated creep stage of rock and enables the prediction of the creep lifespan under different stress levels.
(3) To address the high sensitivity, nonlinearity, and computational expense of rock creep parameter inversion, an improved GA was developed and integrated with FLAC3D. Compared with the standard GA, the improved version achieved significantly faster convergence and higher inversion accuracy, reducing the final L_{2P} error by 22.7% for the CVISC model and 26.0% for the FEVPD model. These results demonstrate that the proposed strategies, including adaptive perturbation, elitism, and dynamic mutation adjustment, are particularly effective for high-cost inversion problems such as those encountered in rock creep parameter identification.

Table 7
Basic parameters of the model in the numerical calculation.

Model	G_1 (GPa)	K (GPa)	φ (°)	c (MPa)	σ^t (MPa)	ρ (kg/m^3)	γ	κ
FEVPD	20.29	27.06	28	6	0.05	2650	0.1287	0.000 766
CVISC	20.29	27.06	28	6	0.05	2650	–	–

Table 8
Parameter inversion results of the Jinping II hydropower station.

Model	ξ	η_M (GPa·h)	η_K (GPa·h)	η_1^{ξ} (GPa·h$^{\xi}$)	G_2 (GPa)	η_2 (GPa·h)	L_{2P} (mm)
FEVPD	0.762	–	–	2189.5	1.153	32.62	0.689
CVISC	–	19907.2	6690.0	–	30.228	–	1.025

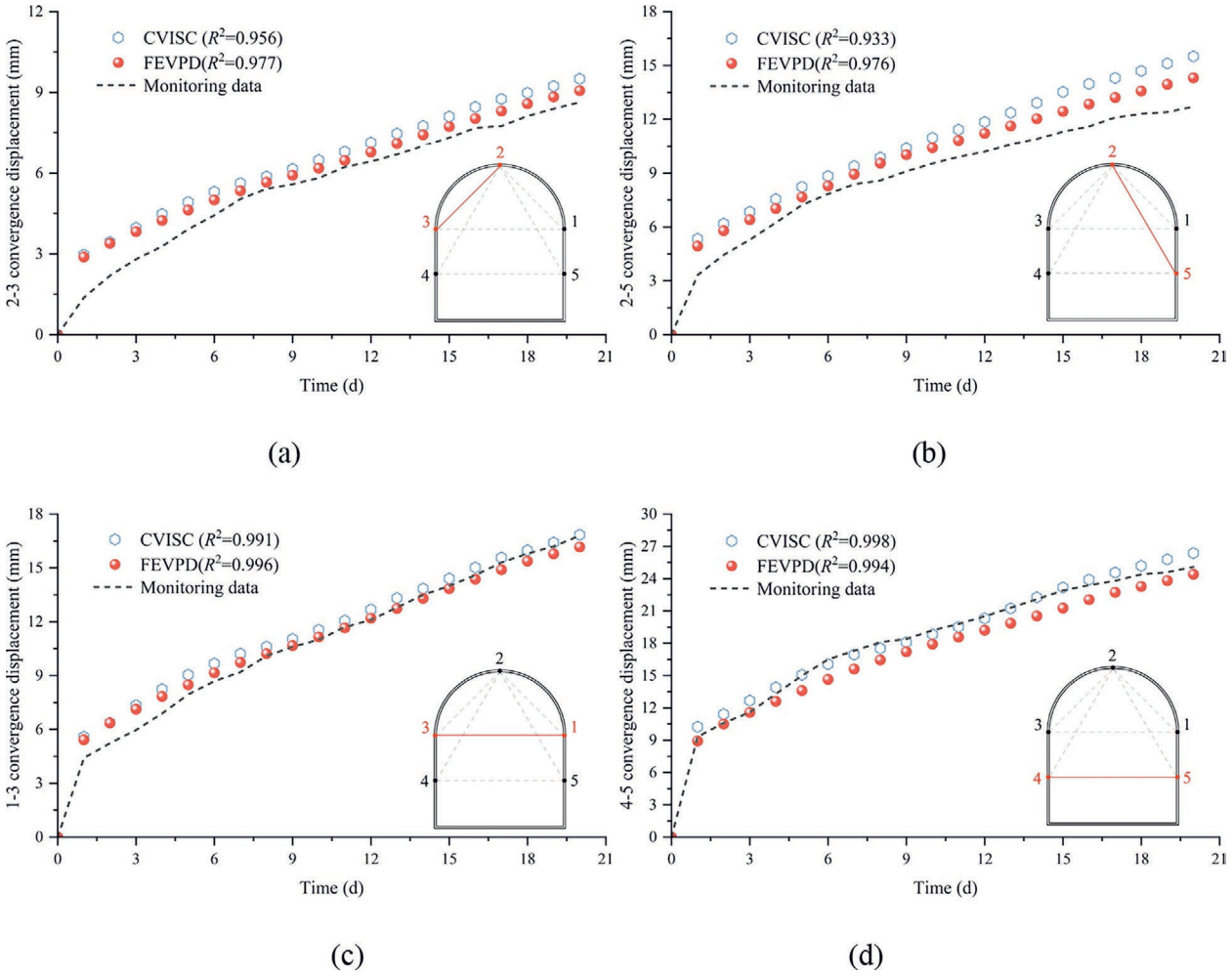

Fig. 15. Comparison of local convergence deformation between numerical simulation and in-situ monitoring. (a) Convergence deformation of 2-3, (b) convergence deformation of 2-5, (c) convergence deformation of 1-3, and (d) convergence deformation of 4-5.

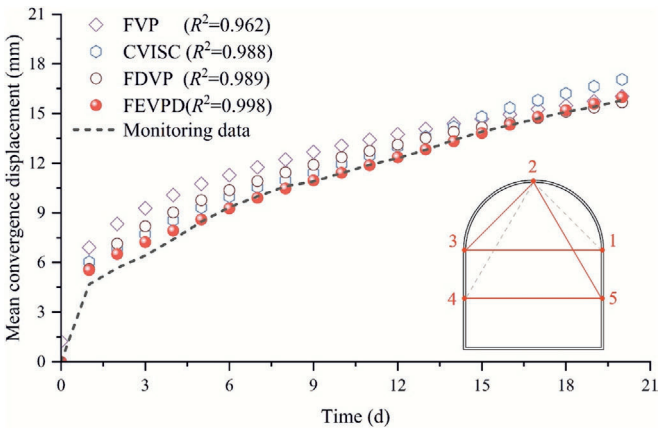

Fig. 16. Comparison of mean convergence deformation between numerical simulation and in-situ monitoring.

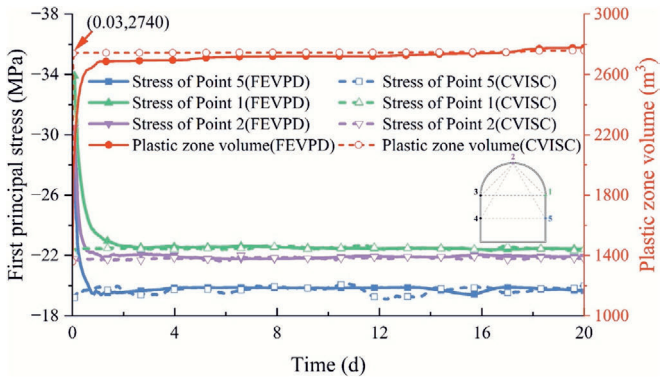

Fig. 17. Evolution curves of the plastic zone volume and the first principal stress.

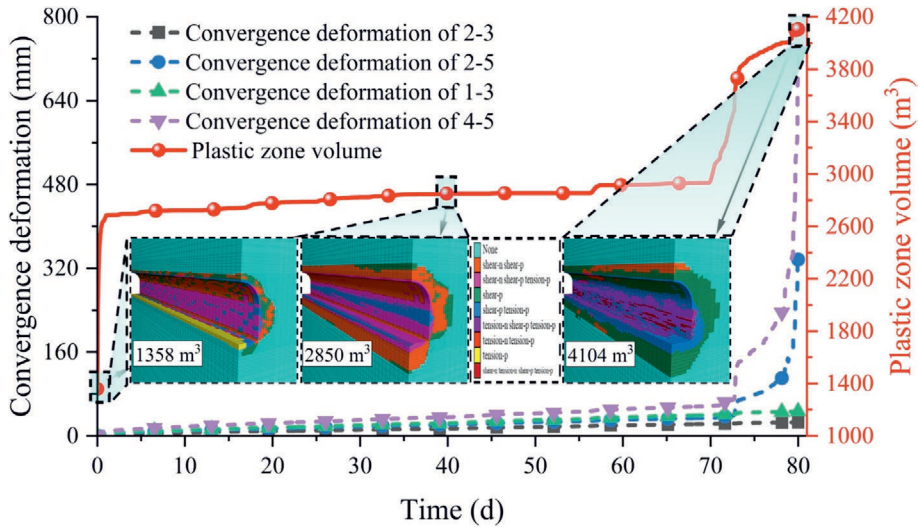

Fig. 18. Long-term stability prediction of the tunnel.

(4) The numerical simulation results confirmed that the FEVPD model captures the time-dependent deformation of the surrounding rock more accurately than the CVISC model. Taking tunnel convergence deformation as an example, the FEVPD model achieved an R^2 value of 0.998 against in-situ monitoring data and yielded an L_{2P} error of 0.689 mm, 32.68% lower than the 1.025 mm error of the CVISC model. Additionally, the FEVPD model was used to predict the long-term stability of the tunnel, revealing the risk of overall instability and failure due to significant local deformation at approximately 70 d.

Data availability

The data that support the findings of this study are available from the corresponding author upon reasonable request.

CRediT authorship contribution statement

Qingzhe Cui: Writing – review & editing, Writing – original draft, Software, Methodology, Data curation. **Fei Wu:** Writing – review & editing, Supervision, Resources, Investigation, Funding acquisition, Conceptualization. **Jianfeng Liu:** Writing – review & editing, Supervision. **Jie Chen:** Writing – review & editing, Supervision. **Cunbao Li:** Writing – review & editing, Supervision. **Renbo Gao:** Writing – review & editing, Supervision. **Shuo Gao:** Writing – review & editing, Supervision. **Yu Wang:** Supervision. **Huiqing Liu:** Supervision. **Tao Ren:** Supervision.

Declaration of competing interest

The authors declare that they have no known competing financial interests or personal relationships that could have appeared to influence the work reported in this paper.

Acknowledgement

This work is supported by the National Natural Science Foundation of China (Grant Nos. 52374078 and U24A20616), the Sichuan-Chongqing Science and Technology Innovation Cooperation Program Project (Grant No. 2024TIAD-CYKJCXX0011), and the Fundamental Research Funds for the Central Universities (Grant No. 2023CDJKYJH021). The author gratefully acknowledges Yingying Guo, M.S., from the College of Veterinary Medicine, Henan Agricultural University, for her helpful language assistance with this work.

Appendix A 3D finite difference formulation of the FEVPD model

The increase in the total deviatoric strain in the FEVPD model is given by

$$\Delta e_{ij} = \Delta e_{ij}^{e} + \Delta e_{ij}^{ve} + \Delta e_{ij}^{vp}. \tag{A1}$$

In the incremental equation, the following expressions are available:

$$\bar{S}_{ij} = \frac{S_{ij}^{O} + S_{ij}^{N}}{2},\ \Delta S_{ij} = S_{ij}^{N} - S_{ij}^{O}, \tag{A2}$$

where the superscripts N and O denote the new and old values, respectively.

According to Eqs. (14) and (A2), the incremental equation of the Hooke body can be expressed as

$$\Delta e_{ij}^{e} = \frac{S_{ij}^{N} - S_{ij}^{O}}{2G_1}. \tag{A3}$$

According to Eqs. (15) and (A2), the incremental equation for the viscoelastic component based on fractal-order derivatives can be expressed as

$$e_{ij}^{\mathrm{ve,N}} = \frac{1}{A}\left[\frac{\xi t^{\xi-1}\Delta t}{4\eta_1^{\xi}}\left(S_{ij}^{\mathrm{O}} + S_{ij}^{\mathrm{N}}\right) + Be_{ij}^{\mathrm{ve,O}}\right], \tag{A4}$$

where $A = 1 + \frac{G_2\xi t^{\xi-1}\Delta t}{2\eta_1^{\xi}}$, and $B = 1 - \frac{G_2\xi t^{\xi-1}\Delta t}{2\eta_1^{\xi}}$.

The constitutive equation for the damaged viscoplastic component can be obtained from Eq. (16):

$$\dot{e}_{ij}^{\mathrm{vp}} = \begin{cases} 0, & F < 0, \\ \frac{F}{2\eta_2}\frac{\partial Q}{\partial \sigma_{ij}}\left(1 - \frac{t}{t_{\mathrm{R}}}\right)^{-\frac{1}{(\gamma+1)}} - \frac{1}{3}e_{\mathrm{vol}}^{\mathrm{vp}}\delta_{ij}, & F \geq 0, \end{cases} \tag{A5}$$

where $e_{\mathrm{vol}}^{\mathrm{vp}} = \frac{F}{2\eta_2}\left(\frac{\partial Q}{\partial \sigma_{11}} + \frac{\partial Q}{\partial \sigma_{22}} + \frac{\partial Q}{\partial \sigma_{33}}\right)$; Q and F are given in Eq. (19).

The three-dimensional incremental equation for the viscoplastic component is obtained from Eq. (A5):

$$\Delta e_{ij}^{\mathrm{vp}} = \begin{cases} 0, & F \leq 0, \\ \frac{F}{2\eta_2}\frac{\partial Q}{\partial \sigma_{ij}}\left(1 - \frac{t}{t_{\mathrm{R}}}\right)^{-\frac{1}{(\gamma+1)}}\Delta t, & F > 0, \end{cases} \tag{A6}$$

For the spherical stress, the following relationship exists:

$$p^{\mathrm{N}} = p^{\mathrm{O}} + K\left(\Delta e_{\mathrm{vol}} - \Delta e_{\mathrm{vol}}^{\mathrm{vp}}\right), \tag{A7}$$

where p^{N} and p^{O} represent the new and old spherical stresses, respectively. The subscript vol denotes a sphere.

Finally, substituting Eqs. (A3), (A4), and (A6) into Eq. (A1) yields the total deviatoric strain increment:

$$\begin{aligned} \Delta e_{ij} &= \Delta e_{ij}^{\mathrm{e}} + \Delta e_{ij}^{\mathrm{ve}} + \Delta e_{ij}^{\mathrm{vp}} \\ &= \begin{cases} \frac{S_{ij}^{\mathrm{N}} - S_{ij}^{\mathrm{O}}}{2G_1} + \frac{1}{A}\left[\frac{\xi t^{\xi-1}\Delta t}{4\eta_1^{\xi}}\left(S_{ij}^{\mathrm{O}} + S_{ij}^{\mathrm{N}}\right) + Be_{ij}^{\mathrm{ve,O}}\right] - e_{ij}^{\mathrm{ve,O}}, & (F < 0), \\ \frac{S_{ij}^{\mathrm{N}} - S_{ij}^{\mathrm{O}}}{2G_1} + \frac{1}{A}\left[\frac{\xi t^{\xi-1}\Delta t}{4\eta_1^{\xi}}\left(S_{ij}^{\mathrm{O}} + S_{ij}^{\mathrm{N}}\right) + Be_{ij}^{\mathrm{ve,O}}\right] - e_{ij}^{\mathrm{ve,O}} \\ \quad + \frac{F}{2\eta_2}\frac{\partial Q}{\partial \sigma_{ij}}\left(1 - \frac{t}{t_{\mathrm{R}}}\right)^{-\frac{1}{(\gamma+1)}}\Delta t, & (F \geq 0). \end{cases} \end{aligned} \tag{A8}$$

According to Eq. (A8),

$$S_{ij}^{N} = \begin{cases} \frac{1}{a}\left[\Delta e_{ij} + bS_{ij}^{\mathrm{O}} + \left(1 - \frac{B}{A}\right)e_{ij}^{\mathrm{ve,O}}\right], & (F < 0) \\ \frac{1}{a}\left[\Delta e_{ij} + bS_{ij}^{\mathrm{O}} + \left(1 - \frac{B}{A}\right)e_{ij}^{\mathrm{ve,O}} - \Delta e_{ij}^{\mathrm{vp}}\right], & (F \geq 0) \end{cases}, \tag{A9}$$

where $a = \frac{1}{2G_1} + \frac{\xi t^{\xi-1}\Delta t}{4A\eta_1^{\xi}}$, and $b = \frac{1}{2G_1} - \frac{\xi t^{\xi-1}\Delta t}{4A\eta_1^{\xi}}$.

At each FLAC3D step, the program first records whether the zone was plastic in the previous step. The stress tensor of intact zones is then calculated using Eq. (A9) as the trial stress, from which FLAC3D derives the principal stresses. According to Eq. (19), if failure occurs, the damage variable is updated, and the trial stress is corrected.

In deep tunnels, delayed deformation involves continuous strain and stress redistribution, thereby rendering the stress state dynamic. Because the creep lifespan is highly sensitive to stress levels, using a constant stress in FLAC3D may misjudge long-term stability. To address this, the creep failure time t_{R} is treated dynamically, and the damage evolution equation (Eq. (5)) is implemented incrementally to capture the cumulative creep damage.

The damage-evolution equation (Eq. (5)) is transformed into the incremental equation:

$$\Delta D = \frac{1}{(\gamma+1)t_{\mathrm{R}}}\left(1 - \frac{t}{t_{\mathrm{R}}}\right)^{-\frac{\gamma}{\gamma+1}}\Delta t. \tag{A10}$$

According to Eq. (6), t_{R} is extended to a three-dimensional form:

$$t_{\mathrm{R}} = \left[\kappa(\gamma+1)\left(\frac{F}{\sigma^*}\right)^{\gamma}\right]^{-1}. \tag{A11}$$

Each calculation step will update t_{R} based on the current trial stress state. Subsequently, the zone stress should be corrected. The deviatoric component is defined as

$$\begin{cases} \sigma_1^{\mathrm{N}} = \widehat{\sigma}_1^{\mathrm{N}} - [\alpha_1\Delta\varepsilon_1^{\mathrm{p}} + \alpha_2(\Delta\varepsilon_2^{\mathrm{p}} + \Delta\varepsilon_3^{\mathrm{p}})], \\ \sigma_2^{\mathrm{N}} = \widehat{\sigma}_2^{\mathrm{N}} - [\alpha_1\Delta\varepsilon_2^{\mathrm{p}} + \alpha_2(\Delta\varepsilon_1^{\mathrm{p}} + \Delta\varepsilon_3^{\mathrm{p}})], \\ \sigma_3^{\mathrm{N}} = \widehat{\sigma}_3^{\mathrm{N}} - [\alpha_1\Delta\varepsilon_3^{\mathrm{p}} + \alpha_2(\Delta\varepsilon_1^{\mathrm{p}} + \Delta\varepsilon_2^{\mathrm{p}})], \end{cases} \tag{A12}$$

where $\alpha_1 = K + \frac{2}{3a}$, and $\alpha_2 = K - \frac{1}{3a}$.

When the zone is in the shear failure state, according to Eq. (A5),

$$\Delta e_i^{\mathrm{vp}} = \lambda^{\mathrm{s}}\frac{\partial Q^{\mathrm{s}}}{\partial \sigma_i}, \quad i = 1, 2, 3, \tag{A13}$$

where $\lambda^{\mathrm{s}} = \frac{F}{2\eta_2}\left(1 - \frac{t}{t_{\mathrm{R}}}\right)^{-\frac{1}{(\gamma+1)}}\Delta t$.

Substituting the shear plastic potential function ($Q^{\mathrm{s}} = \sigma_1 - \sigma_3 N_\psi$) into Eq. (A13) yields the following plastic strain increment:

$$\begin{cases} \Delta e_1^{\mathrm{vp}} = \lambda^{\mathrm{s}}, \\ \Delta e_2^{\mathrm{vp}} = 0, \\ \Delta e_3^{\mathrm{vp}} = -\lambda^{\mathrm{s}}N_\psi. \end{cases} \tag{A14}$$

The shear yield function is expressed as

$$f^{\mathrm{s}} = \widehat{\sigma}_1^{\mathrm{N}} - \widehat{\sigma}_3^{\mathrm{N}}N_\varphi + 2c\sqrt{N_\varphi}. \tag{A15}$$

By substituting Eqs. (A14) and (A15) into Eq. (A12), the actual stress can be obtained as follows:

$$\begin{cases} \sigma_1^{\mathrm{N}} = \hat{\sigma}_1^{\mathrm{N}} - \lambda^{\mathrm{s}}\left(\alpha_1 - \alpha_2 N_\psi\right), \\ \sigma_2^{\mathrm{N}} = \hat{\sigma}_2^{\mathrm{N}} - \lambda^{\mathrm{s}}\alpha_2\left(1 - N_\psi\right), \\ \sigma_3^{\mathrm{N}} = \hat{\sigma}_3^{\mathrm{N}} - \lambda^{\mathrm{s}}\left(\alpha_2 - \alpha_1 N_\psi\right). \end{cases} \tag{A16}$$

When the zone undergoes tensile failure, according to Eq. (A5),

$$\Delta e_i^{\mathrm{vp}} = \lambda^{\mathrm{t}}\frac{\partial Q^{\mathrm{t}}}{\partial \sigma_i} \quad i = 1, 2, 3, \tag{A17}$$

where

$$\lambda^{\mathrm{t}} = \frac{F}{2\eta_2}\left(1 - \frac{t}{t_{\mathrm{R}}}\right)^{-\frac{1}{(\gamma+1)}}\Delta t. \tag{A18}$$

By substituting the tensile plastic potential function ($Q^{\mathrm{t}} = -\sigma_3$) into Eq. (A17), the plastic strain increment is

$$\begin{cases} \Delta e_1^{\mathrm{vp}} = 0, \\ \Delta e_2^{\mathrm{vp}} = 0, \\ \Delta e_3^{\mathrm{vp}} = -\lambda^{\mathrm{t}}. \end{cases} \tag{A19}$$

The tensile yield function is expressed as

$$f^{\mathrm{t}} = \sigma^{\mathrm{t}} - \widehat{\sigma}_3^{\mathrm{N}}. \tag{A20}$$

By substituting Eqs. (A19) and (A20) into Eq. (A12), the actual stress can be obtained as follows:

$$\begin{cases} \sigma_1^{\mathrm{N}} = \hat{\sigma}_1^{\mathrm{N}} + \lambda^{\mathrm{t}}\alpha_2, \\ \sigma_2^{\mathrm{N}} = \hat{\sigma}_2^{\mathrm{N}} + \lambda^{\mathrm{t}}\alpha_2, \\ \sigma_3^{\mathrm{N}} = \hat{\sigma}_3^{\mathrm{N}} + \lambda^{\mathrm{t}}\alpha_1. \end{cases} \tag{A21}$$

Appendix B Computational accuracy and efficiency of the improved GA

The section evaluated the proposed GA against a standard GA using the FEVPD model under identical settings (population = 50, generations = 100, and objective $L_{2\mathrm{P}}$). The tests were performed on an Intel Core i9-14900 K (3.20 GHz). Each individual triggered one numerical simulation (≈13.28 s); therefore, a full 100 × 50 run was ≈18.4 h.

Accuracy. Fig. B1 (six runs) shows a lower converged mean error for the improved GA (0.753 mm) than the standard GA (1.009 mm), i.e., −25.4% at the same evaluation budget. The improved GA also reaches <0.9 mm during evolution, whereas the baseline does not within 100 generations.

Efficiency (time-to-target). For a threshold $L_{2\mathrm{P}} \leq 1.1$ mm, the standard GA converged at generation 44 (≈8.1 h), whereas the improved GA converged at generation 9 (≈1.7 h), yielding an ≈4.8 × speedup (≈79% less time). For a stricter threshold of $L_{2\mathrm{P}} \leq 0.9$ mm, the standard GA had difficulty converging within 100 generations, whereas the improved GA converged at approximately generation 34 (≈6.3 h).

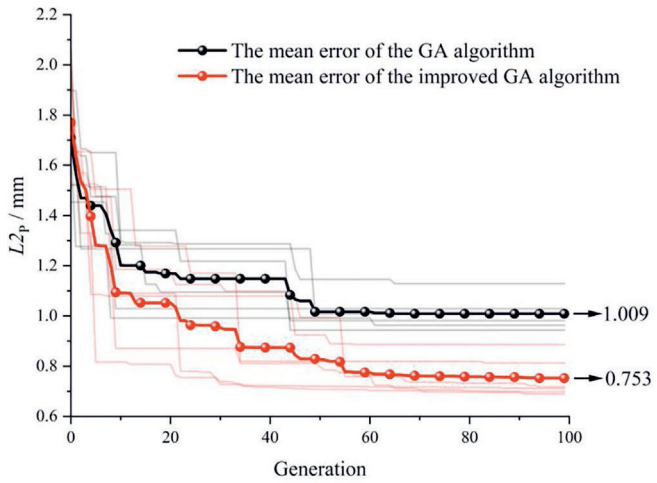

Fig. B1. Error comparison between the improved GA and the standard GA.

Overhead of the GA code. The CPU time of the algorithm itself was negligible relative to simulation time (≲0.01% of wall-time); see Table B1.

Table B1
Comparison table of simulation CPU and algorithm CPU times.

	Old GA	Improved GA
Total number of individuals	5000	5000
Total CPU time for numerical simulations (s)	67 093.8	66 412.5
Total CPU time for the algorithm (s)	1.3	5.2
CPU time per simulation (s)	13.42	13.28
CPU time per algorithm iteration (s)	0.000 26	0.001 04

References

Alessandro, C., & Eurípedes, V. (2023). A thermodynamic modeling of creep in rock salt. *International Journal of Rock Mechanics and Mining Sciences, 162*, 105298.

An, J. S., Kang, K. N., Choi, J. Y., Sung, W. S., Suy, V., & Song, K. I. (2020). Tunnel back analysis based on differential evolution using stress and displacement. *Advances in Civil Engineering, 2020*(1), 8156573.

Barla, G., Debernardi, D., & Sterpi, D. (2012). Time-dependent modeling of tunnels in squeezing conditions. *International Journal of Geomechanics, 12*(6), 697–710.

Bonini, M., Debernardi, D., Barla, M., & Barla, G. (2007). The mechanical behaviour of clay shales and implications on the design of tunnels. *Rock Mechanics and Rock Engineering, 42*(2), 361–388.

Cai, W., Chen, W., & Xu, W. X. (2016). Characterizing the creep of viscoelastic materials by fractal derivative models. *International Journal of Non-Linear Mechanics, 87*, 58–63.

Chang, X. Y., Wang, H., & Zhang, Y. M. (2023). Back analysis of rock mass parameters in tunnel engineering using machine learning techniques. *Computers and Geotechnics, 163*, 105738.

Chen, B. R., & Feng, X. T. (2008). Universal viscoelastoplastic combination model and its engineering applications. *Chinese Journal of Rock Mechanics and Engineering, 27*, 1028–1035 (in Chinese).

Chen, B. R., Zhao, X. J., Feng, X. T., Zhao, H. B., & Wang, S. Y. (2013). Time-dependent damage constitutive model for the marble in the Jinping II hydropower station in China. *Bulletin of Engineering Geology and the Environment, 73*(2), 499–515.

Cui, Q. Z., Hou, R. B., Li, Z. H., Du, F., Chen, X., Zhang, B. Y., & Li, L. L. (2025a). Time-dependent behavior of deep roadway surrounding rock considering damage induced by excavation and mining disturbances: Experiments, modeling, and simulation. *International Journal of Mining Science and Technology* (in press).

Cui, Q. Z., Wu, F., Liu, J. F., Chen, J., Li, C. B., Gao, R. B., Gao, S., Liu, H. Q., & Ren, T. (2025b). A variable fractal-order rock salt creep model with full-time domain memory effect and its application in salt cavern hydrogen storage. *Energy, 338*, 138870.

Cui, Q. Z., Wu, F., Wang, L. T., Liu, J. F., Chen, J., Li, C. B., Liu, H. Q., & Gao, R. B. (2025c). A rock elasto-visco-plastic creep model fully considering the effect of time-dependent damage. *Computers and Geotechnics, 187*, 107490.

Debernardi, D., & Barla, G. (2009). New viscoplastic model for design analysis of tunnels in squeezing conditions. *Rock Mechanics and Rock Engineering, 42*(2), 259–288.

Feng, X. T., Chen, B. R., Yang, C. X., Zhou, H., & Ding, X. L. (2006). Identification of visco-elastic models for rocks using genetic programming coupled with the modified particle swarm optimization algorithm. *International Journal of Rock Mechanics and Mining Sciences, 43*(5), 789–801.

Gao, R. B., Wu, F., Chen, J., Zhu, C., & Ji, C. X. (2022). Study on creep characteristics and constitutive model of typical argillaceous salt rock

in energy storage caverns in China. *Journal of Energy Storage, 50*, 104248.
Ghorbani, E., Moosavi, M., Hossaini, M. F., Assary, M., & Golabchi, Y. (2021). Determination of initial stress state and rock mass deformation modulus at Lavarak HEPP by back analysis using ant colony optimization and multivariable regression analysis. *Bulletin of Engineering Geology and the Environment, 80*(1), 429–442.
Gong, Y. P., Kou, Y. G., Yue, Q., Zhuang, X. Y., Valizadeh, N., Qin, F., Wang, Q., & Rabczuk, T. (2025). A phase-field study on thermo-mechanical coupled damage evolution and failure mechanisms of sintered silver interconnections. *Engineering Fracture Mechanics, 320*, 111039.
He, Q. C., Wu, F., & Gao, R. B. (2022). Nonlinear creep-damage constitutive model of surrounding rock in salt cavern reservoir. *Journal of Energy Storage, 55*, 105520.
Herrmann, R. (2014). *Fractional calculus: An introduction for physicists*. Singapore: World Scientific Publishing.
Holland, J. H. (1975). *Adaptation in natural and artificial systems*. Ann Arbor: University of Michigan Press.
Hou, R. B., Cui, Q. Z., Guo, Y. Y., Shi, Y. K., & Fu, J. W. (2024). A new elasto-visco-plastic damage model and numerical simulation method used for time-dependent behavior prediction of deep tunnel. *Computers and Geotechnics, 168*, 106129.
ITASCA (2017). *FLAC3D (Version 6. 0) users manual, Itasca Consulting*. Minneapolis: Group Inc..
Kabwe, E., Karakus, M., & Chanda, E. K. (2020a). Creep constitutive model considering the overstress theory with an associative viscoplastic flow rule. *Computers and Geotechnics, 124*, 103629.
Kabwe, E., Karakus, M., & Chanda, E. K. (2020b). Isotropic damage constitutive model for time-dependent behaviour of tunnels in squeezing ground. *Computers and Geotechnics, 127*, 103738.
Kachanov, L. M. (1958). Rupture time under creep conditions. *International Journal of Fracture, 97*(1), 11–18.
Kilbas, A. A., Srivastava, H. M., & Trujillo, J. J. (2006). *Theory and applications of fractional differential equations*. Amsterdam: Elsevier Science B.V.
Kong, F. C., Lu, D. C., Ma, C., Shen, C. P., Yang, X. D., & Du, X. L. (2023). Fractional viscoelastic solution of stratum displacement of a shallow tunnel under the surface slope condition. *Underground Space, 10*, 233–247.
Lemaitre, J. (1996). *A course on damage mechanics*. Berlin: Springer.
Li, H., Ma, H. L., Yang, C. H., Wang, X., & Daemen, J. J. K. (2024a). Creep-fatigue model of rock salt based on a fractal-order derivative considering thermo-mechanical damage. *Computers and Geotechnics, 174*, 106605.
Li, J., Hou, S. B., Jiang, Y. L., Fu, H. L., & Hu, K. X. (2025). A constitutive model of rock based on strain cone surface and the parameter calibration method with high efficiency. *Computers and Geotechnics, 177*, 106876.
Li, T. B., Chen, C., Peng, F., Ma, C. C., Li, M., & Wang, Y. X. (2024b). Creep damage constitutive model of rock based on the mechanisms of crack-initiated damage and extended damage. *Underground Space, 18*, 295–313.
Liang, C., Liu, J. F., Yang, J. X., Xu, H. N., Chen, Z. W., & Ran, L. N. (2024). A creep model for ultra-deep salt rock considering thermal-mechanical damage under triaxial stress conditions. *Journal of Rock Mechanics and Geotechnical Engineering, 16*(2), 588–596.
Liu, C., Zhang, D. L., Zhang, S. L., Fang, Q., & Sun, Z. Y. (2023). Long-term mechanical analysis of tunnel structures in rheological rock considering the degradation of primary lining. *Underground Space, 10*, 217–232.
Liu, J., Zeng, X. H., Zheng, W. Q., Lai, H. P., Wang, Y. L., Wang, F., & Qiu, H. (2025). Dynamic behavior of a running crack crossing mortar-granite interface with different interface inclinations. *Engineering Fracture Mechanics, 314*, 110705.
Luo, W., Le, J. L., Rasoolinejad, M., & Bažant, Z. P. (2021). Coefficient of variation of shear strength of RC beams and size effect. *Journal of Engineering Mechanics, 147*(2), 04020144.
Lyu, C., Liu, J. F., Ren, Y., Liang, C., & Liao, Y. L. (2021). Study on very long-term creep tests and nonlinear creep-damage constitutive model of salt rock. *International Journal of Rock Mechanics and Mining Sciences, 146*, 104873.
Mahmoudi, M., & Rajabi, A. M. (2020). Application of numerical back analysis for determination of soil mass specifications during tunnel construction. *Arabian Journal of Geosciences, 13*(19), 990.
Majdi, A., & Beiki, M. (2010). Evolving neural network using a genetic algorithm for predicting the deformation modulus of rock masses. *International Journal of Rock Mechanics and Mining Sciences, 47*(2), 246–253.
Marquardt, D. W. (1963). An algorithm for least-squares estimation of nonlinear parameters. *Journal of the Society for Industrial and Applied Mathematics, 11*(2), 431–441.
Perzyna, P. (1966). Fundamental problems in viscoplasticity. *Advances in Applied Mechanics, 9*, 243–377.
Samaniego, E., Anitescu, C., Goswami, S., Nguyen-Thanh, V. M., Guo, H., Hamdia, K., Zhuang, X., & Rabczuk, T. (2020). An energy approach to the solution of partial differential equations in computational mechanics via machine learning: Concepts, implementation and applications. *Computer Methods in Applied Mechanics and Engineering, 362*, 112790.
Sun, J. L., Wang, F., Wang, X. L., & Wu, X. (2021). A quantitative evaluation method based on back analysis and the double-strength reduction optimization method for tunnel stability. *Advances in Civil Engineering, 2021*, 1–14.
Wang, C., Ma, G. W., Zhao, J., & Soh, C. K. (2004). Identification of dynamic rock properties using a genetic algorithm. *International Journal of Rock Mechanics and Mining Sciences, 41*, 490–495.
Wang, H. B., Wang, F. M., Guo, C. C., Qin, L., Liu, J., & Qu, T. M. (2025). Experimental investigation on the failure characteristic and synergistic load-bearing mechanism of multi-layer linings for deep soft rock tunnels. *Underground Space, 20*, 259–276.
Wang, J. B., Zhang, Q., Song, Z. P., Feng, S. J., & Zhang, Y. W. (2022). Nonlinear creep model of salt rock used for displacement prediction of salt cavern gas storage. *Journal of Energy Storage, 48*, 103951.
Wu, F., Ji, C. X., Liu, J., Gao, R. B., Li, C. B., Zou, Q. L., & Chen, J. (2023a). Study on visco-elastoplastic fractional creep model of surrounding rock of salt cavern gas storage. *Journal of Energy Storage, 67*, 107606.
Wu, F., Yu, Q. L., & Liu, C. W. (2022). Creep characteristics and constitutive model of bio-based concrete in aqueous environment. *Construction and Building Materials, 320*, 126213.
Wu, J., Wang, W., Cao, Y. J., Liu, S. F., Zhang, Q., & Chu, W. J. (2023b). A novel nonlinear fractional viscoelastic–viscoplastic damage creep model for rock-like geomaterials. *Computers and Geotechnics, 163*, 105726.
Yang, C., Zhu, Z. J., Wang, J., Deng, H. F., Huang, D., & Tang, J. T. (2024). Damaged creep constitutive models of rock-like materials containing multiple flaws and their relationships to those of the intact materials. *Theoretical and Applied Fracture Mechanics, 130*, 104306.
Yang, W. D., Wang, X. P., Ivanović, A., & Zhang, X. (2023). Coupled analytical solutions for circular tunnels considering rock creep effects and time-dependent anchoring forces in prestressed bolts. *Tunnelling and Underground Space Technology, 134*, 104954.
Yin, W., Wang, X. Y., Zheng, S., Zhang, K., & Zhang, F. R. (2024). Triaxial creep test and damage model study of layered red sandstone under freeze-thaw cycles. *Case Studies in Construction Materials, 21*, e03785.
Zhang, J. Z., Zhou, X. P., & Yin, P. (2019). Visco-plastic deformation analysis of rock tunnels based on fractional derivatives. *Tunnelling and Underground Space Technology, 85*, 209–219.
Zhao, C. W., Zhou, H., Zhang, C. Q., Liu, W. B., Li, L. Y., Liu, Z. B., & Huo, Z. Y. (2025). Creep-slip behaviors of surrounding rocks in a water diversion tunnel considering strike-slip and dip-slip scenarios. *Tunnelling and Underground Space Technology, 158*, 106405.
Zhao, Y. L., Wang, Y. X., Wang, W. J., Wan, W., & Tang, J. Z. (2017a). Modeling of non-linear rheological behavior of hard rock using triaxial rheological experiment. *International Journal of Rock Mechanics and Mining Sciences, 93*, 66–75.
Zhao, Y. L., Zhang, L. Y., Wang, W. J., Wan, W., Li, S. Q., Ma, W. H., & Wang, Y. X. (2017b). Creep behavior of intact and cracked limestone under multi-level loading and unloading cycles. *Rock Mechanics and Rock Engineering, 50*(6), 1409–1424.
Zheng, C. T., Zhu, X. Y., & Zhang, Z. Q. (2024). Damage evolution of tunnel lining under creep action considering interlayer effect in gently inclined layered surrounding rock. *Engineering Failure Analysis, 162*, 108392.
Zheng, Y., Chen, C. X., Meng, F., Liu, T. T., & Xia, K. Z. (2020). Assessing the stability of rock slopes with respect to flexural toppling failure using a limit equilibrium model and genetic algorithm. *Computers and Geotechnics, 124*, 103619.

Zhou, J. X., Zhang, J. W., Wang, J. A., Li, F., & Zhou, Y. (2022). Research on nonlinear damage hardening creep model of soft surrounding rock under the stress of deep coal resources mining. *Energy Reports, 8*, 1493–1507.

Zienkiewicz, O. C., & Cormeau, I. C. (1974). Visco-plasticity—plasticity and creep in elastic solids—a unified numerical solution approach. *International Journal for Numerical Methods in Engineering, 8*(4), 821–845.